Pergamon

Int. J. Solids Structures Vol. 31, No. 19, pp. 2679–2708, 1994

0020–7683/94 $7.00 + .00

0020–7683(94)E0046–X

ANALYSIS OF VICKERS INDENTATION

A. E. GIANNAKOPOULOS†, P.-L. LARSSON and R. VESTERGAARD
Department of Solid Mechanics, Royal Institute of Technology, S-10044 Stockholm, Sweden

(*Received* 19 *November* 1993; *in revised form* 8 *February* 1994)

Abstract—Indentation tests have for a long time been a standard method for material characterization as they provide an easy, inexpensive, non-destructive and objective method of evaluating basic properties from small volumes of materials. Besides hardness, recently also aspects of, for example, toughness and residual stresses have been advantageously investigated by indentation. Sharp indentation tests such as Vickers, Berkovich and Knoop lack however a solid mechanical foundation. The present paper aims mainly to explore the theoretical foundation for the commonly used Vickers test. The investigated types of constitutive behavior include isotropic linear elasticity and plasticity. The influence of large elastoplastic deformations was also assessed. Extensive computation was required, based on the finite element method. In addition, the analysis was compared with depth-sensing indentation experiments. The results put forward explanations of hardness formulae for many standard materials such as metals, as well as the stress and deformation analysis relating to the Vickers indentation test.

1. INTRODUCTION

Indentation tests have for a long time been a standard method for material characterization [see, for example, Tabor (1951); Mott (1956)]. Not only hardness *per se* (maximum applied force divided by the residual indentation area), but also other material properties (e.g. stiffness and yield strength) may be inferred from examining the load versus the indentation shapes of various materials. The hardness test consists of loading an indenter made of diamond or any other hard material and pressing it into the surface of a softer material to be examined. The further into the material the indenter sinks (for a given load), the softer the material is and the lower its yield strength. Sharp indenters are usually in the shape of pyramids of square base (Vickers), triagonal base (Berkovich) and rhomboid base (Knoop), or in conical shape (Rockwell). Hardness tests are the most commonly used non-destructive testing procedures in the metal industry and in research because they provide an easy, inexpensive and reliable method of evaluating basic properties of developed or new materials. The hardness test indenter is so small that it scarcely damages the bulk material, therefore, it can be used for routine batch tests on small samples of materials to ascertain that they are up to specifications on yield without damaging them. Furthermore, for brittle materials, for example ceramics, indentation can be a good alternative test because it subsidizes the need for expensive tensile specimens which in some cases are extremely difficult to test due to their high stiffness and brittleness.

In addition, sharp indentation tests also serve to initiate and control fracture tests in brittle materials. Much effort has been devoted to fracture toughness determination [e.g. Anstis *et al.* (1981); Evans and Charles (1976); Lawn *et al.* (1980)]. Other applications that refer to, or use indirectly, the Vickers hardness include abrasive wear problems, armor plating, machining, etc. Most tests are of "static" type, however, several dynamic tests are also available. The development of an ultra-low load indentation system (nano-indenter) (Pethica *et al.*, 1983) increased the use of hardness testing on small volumes of material, for example, electronics, corrosion protection coatings, paints and wear-resistant coatings for tooling and other tribological applications. Another important aspect of the nano-indenter is the continuous reading of the applied load versus the indentation depth during the whole indentation cycle which also enables extraction of information about the elastic properties of the material.

† Author to whom correspondence should be addressed.

Numerous reports and published papers exist on sharp indentation experiments done on many materials like metals, polymers, ceramics, etc. (perhaps the most well known being the standard books of Tabor, 1951 and Johnson, 1985), a fact that indicates the importance of sharp indentation procedures in the evaluation of mechanical properties. The philosophy behind the analysis of such tests is to estimate certain material properties without considering the detailed solution in the entire body. With the exception of the conical indenter which leads to an axisymmetric problem studied thoroughly by Laursen and Simo (1992), the current analytical methods rely heavily on simplifications, at best, or speculation, at worst, about the stress fields and the deformation patterns, requiring curve-fitting from extensive experimentation. Existing methods for evaluating mechanical properties such as hardness can be better classified as semi-empirical laws which need a more sound verification.

The mechanical analysis requires a formulation of the sharp indentation problem which is unavoidably three-dimensional and at first look seems quite impossible to solve, mainly for the following additional reasons: (1) it involves large geometric nonlinearities due to imposed large rotations and high strains at the tip of the indenter; (2) it introduces a difficult contact problem at the interface of the indenter and the body; (3) it predicts stress concentrations of a complicated type close to the edges of the indenter; (4) it involves scale problems since the indented body is modeled as semi-infinite. Moreover, the formulation of the problem is further complicated as material nonlinearities prevail due to various dissipative mechanisms such as plasticity, phase transformation, microcracking and in the presence of residual stresses. The properties of the indenter, such as its shape (e.g. triagonal or tetragonal pyramid), are also very important to the analysis. The combination of all these effects makes the problem formidable to be addressed analytically, and for this reason it was left unsolved in the past. Today's computational capacity is, however, sufficient for a detailed investigation of the important features of sharp indentation tests, and this is what the present and sequential works aim at. The present paper concerns the analysis of the commonly used Vickers hardness test, in particular for metals and other elastoplastic materials.

In what follows, we present the method and the acquired results that clarify the scope of this investigation. Remembering the nonlinearities involved, we relied heavily upon the use of finite elements (FEM). To this end considerable theoretical and numerical experience was drawn from especially the work on the Brinell test (spherical indenter) by Hill *et al.* (1989) and Storåkers and Larsson (1993) but also from earlier attempts to attack the Vickers hardness test numerically by, for example, Wang and Bangert (1993) and Olaf (1993).

However, much important research still remains to be done regarding the analysis of sharp indentation tests. The material nonlinearity and other dissipating effects (e.g. friction) modeled by the constitutive equations should include anisotropy to account for materials like fiber and layered composites, and wood. Residual stresses may arise from thermal or from mechanical treatment (e.g. polishing) of the surface, increasing or decreasing the actual hardness. Dynamic effects could be due to the indenter's kinetic energy for very fast tests, or due to viscous forces for very slow tests at elevated temperatures. More complicated problems could include the influence of a thin layer or other material inhomogeneities on the surface of the indented body. Repeated load–unload indentation could also be important when investigating the fretting fatigue of materials.

2. PROBLEM FORMULATION

In Fig. 1, the geometry of the Vickers indentation test is shown schematically. The true projection of the contact area is in general different from the simple square shown in Fig. 1(a), as will be shown in the following. We assume a rigid indenter penetrating a homogeneous, isotropic, rate independent, semi-infinite body. Due to the eight-fold symmetry of the deformation, which is experimentally observed in many materials, only one eighth of the body needs to be modeled, as indicated by the shaded part of Fig. 1(a), thus dramatically reducing the computational cost. In case of configuration instability or

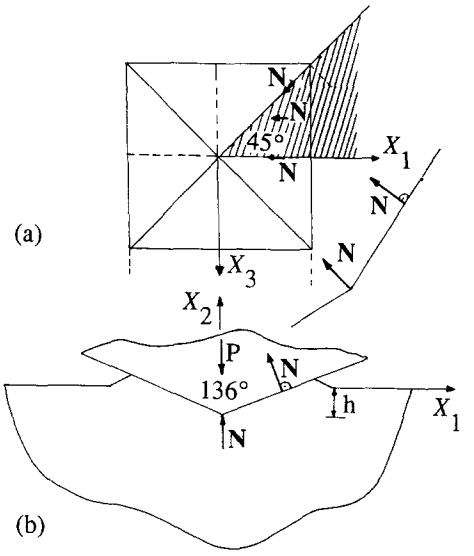

Fig. 1. Schematic of the geometry of the Vickers test; (a) top view, (b) side view.

material anisotropy, the whole body has to be modeled. Quasi-static, isothermal analysis was carried out throughout this work. The indentation is assumed to take place so that dynamic effects, mainly due to the kinetic energy of the indenter, can be ignored. Bulk constitutive behavior was assumed for the indented body, which means that all our results are meaningful for indentation depth h, that is much higher than the characteristic microstructural size of the indented material (e.g. grain size).

The indentation of the half space is a nonlinear problem, since as for one thing the extent of the contact area is not known *a priori*. A penalty approach method is used here for the contact pressure definition where the contact pressure at a point on the deformed surface p_c, is given as a function of the interpenetration h_c, of the contacting surfaces as predicted in the absence of the contact constraint

$$\begin{aligned} p_c &= 0\,;(h_c < 0) \\ p_c &= \bar{k}h_c\,;(h_c \geqslant 0), \end{aligned} \tag{1}$$

where $\bar{k}$ is a large penalty coefficient resembling a very stiff spring constant. The limiting case of eqn (1), as $\bar{k} \to \infty$, corresponds to the Signorini type of contact boundary condition (zero contact traction at the contact area perimeter). No friction was accounted for in the present formulation. This seems to be a reasonable assumption, as previous indentation results (Bower *et al.*, 1993), showed no essential influence of friction on the contact analysis of spherical indenters. Experimental results by Li *et al.* (1993) showed that the indenter/specimen interfacial friction has a minimal effect in the high-test load regime of Vickers indentation testing, but has a significant effect on the low-test load regime.

A key issue for the accuracy and efficiency of the FEM computations was the development of an appropriate mesh which approximated the semi-infinite body. To this end, a general three-dimensional mesh generation program was developed that could fully control the element density and the element transition ratio, as well as the possibility of different pyramidal indenters. The type of FEM mesh used in our analysis is shown in Fig. 2. The patched multi-block technique was used where the physical domain was divided into a set of subdomain blocks joined precisely together along their common boundaries. On a given grid, short-wave errors are damped out faster than long-wave errors. The hierarchy of mesh sizes reduces the amplitude of high frequency errors which cannot be approximated on the adjacent coarser grid. The boundary conditions are transferred to the solution through the coarser grid to further eliminate error components with larger wavelengths. In this way the basic source of numerical error which is due to the boundary conditions at infinity can be

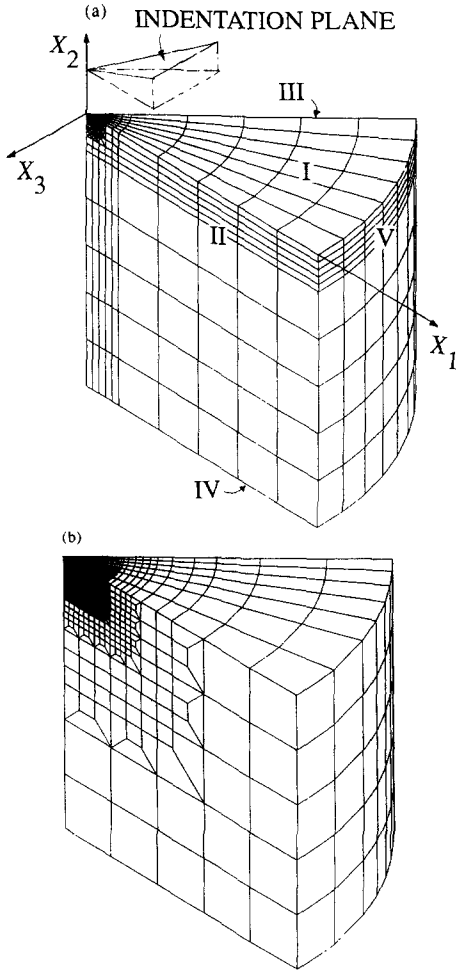

Fig. 2. The FEM mesh used mainly in the linear elastic three-dimensional analysis of the Vickers indentation problem; (a) general view, (b) detail of the mesh at the contact region. 8524 eight-noded elements (9914 nodes).

suppressed. In relation to Fig. 2(a), the indented body is bounded by five characteristic surfaces: the planes I, II, III, IV and the cylindrical surface V. The nodes of planes II, III and IV can deform only in their own planes. Plane I is the indented surface which includes the contact elements. Plane IV (at a depth r_V from the idented surface) has zero vertical displacements. The surface V (at a distance r_H from the indentation axis) is traction free. The very fine mesh division close to the indenter's tip allows a good resolution of the contact area. The figures that contain the isocontours of various mechanical variables will be presented for the planes I, II, III (the top and the two sides shown in Figs 1 and 2(a)). The mesh independency of the results was additionally checked by solving some problems with rounded edges of the indenter. It can be easily argued that the far field solution must approach the Boussinesq solution. The FEM meshes were constructed to engulf the solution near the contact region by the elastic Boussinesq solution. In the elastic analysis, and in view that no Saint-Venant principle is available for the contact problem, the outer boundaries were taken at least about 50 times the maximum contact length away from the indented area. Therefore, boundary value errors are introduced in the FEM approximate solution due to the imposed boundary conditions applied on the computational mesh. Using the elastic solution of a point force acting normal to the surface of a half space, the maximum error in traction (close to the indentation plane) is estimated to be

$$e_t = \frac{3P}{2\pi r_H^2}, \tag{2}$$

and the maximum error in the displacement

$$e_d = \frac{P}{4\pi r_V}\left[\frac{4(1-\nu^2)}{E} + \frac{2(1+\nu)}{E}\frac{r_V}{(r_H^2+r_V^2)^{1/2}}\right]. \tag{3}$$

The traction error (2), due to the (three-dimensional) eight-noded element type used in this analysis introduces a numerical displacement error

$$e_d^{FEM} = e_t\frac{h_H}{E}, \tag{4}$$

where h_H is the typical horizontal size of the elements close to the indented surface. The displacement error (3), in turn, introduces a traction error

$$e_t^{FEM} = e_d\frac{E}{h_V}, \tag{5}$$

where h_V is the typical vertical size of the elements close to the boundary. Comparable errors can be predicted, if $r_H/r_V \leqslant 1/5$. Notice that it is very important for the solution accuracy that the mesh be elongated beneath, and finer near, the contact area. An alternative would have been to use the Boussinesq tractions at the boundary. The mesh used in the elastoplastic analysis was constructed according to these guidelines to further minimize the errors due to the imposed finite boundary conditions.

Extensive testing of the mesh was undertaken to assess the element type, the node density, the element layout and the far field conditions which have to conform to the well known Boussinesq solution of a point force normal to the surface of a semi-infinite elastic solid. In order to do that, we selected as a benchmark problem the flat axisymmetric punch on a semi-infinite, linear elastic, isotropic material with no friction at the interface. An analytic solution by Sneddon (1945) exists for this problem. Our numerical results proved to be in excellent agreement with the analytic ones, both for the displacements and the stresses. The singularity around the sharp edge was well captured within one element size distance. The contact area covered 12 elements.

Based on the circular punch analysis, the mesh shown in Fig. 2 was constructed for the Vickers analysis with the following characteristics; 8524 eight-noded isoparametric block elements (trilinear interpolation functions) and 9914 nodes. Sufficiently high load (of the order Eh^2; E is the material Young's modulus and h is the indentation depth) was applied incrementally to permit good resolution of the contact area. In the elastic analysis, the contact area resolution was with at least 12 elements in all directions. In the elastoplastic analysis, the contact area covered at least six elements in all directions which was adequate, as indicated by the converging of all mechanical variables. Full numerical integration was used for the elastic behavior. Reduced integration was used to improve plastic incompressibility, and the accuracy was also tested by full integration calculations. No mesh instabilities (e.g. "hourglass" modes) were observed in our computations. Full Newton–Raphson method was used for the elastoplastic analysis.

For the Vickers indentation, the isotropic elastic analysis was performed using Hooke's law within small strain formulation and within a hypoelastic formulation in order to examine the influence of finite deformations. The other class of constitutive behavior examined was the Prandtl–Reuss model for incrementally elastoplastic, rate independent materials with isotropic hardening. Small and large strain elastoplastic calculations were performed for elastic–perfectly plastic, as well as for linear strain hardening materials. Loading and unloading was considered.

Regarding the finite deformation analysis, the question appears whether to use a hypoelastic or hyperelastic formulation in the elastic part of the constitutive relation. For this matter, a comparison was made between the elastoplastic cone indentation results given by Bhattacharya and Nix (1988a,b) for the hypoelastic formulation and Laursen and Simo

(1992) for the hyperelastic formulation. Although some discrepancies in these results were found for indentation of thin films on semi-infinite substrates, this was, as discussed by Laursen and Simo (1992), mainly due to differences in meshing. In fact for bulk materials, results like hardness, load–indentation depth curves and surface displacements were essentially the same, regardless of what formulation was used for the elastic part of the constitutive equation. Therefore, due to the smaller amount of computational time required and due to lack of knowledge of the hyperelastic potentials of the examined elastoplastic materials, we chose to perform our calculations using the hypoelastic formulation. The ABAQUS (1989) general purpose program was used. The small strain elastic computations were faster by a factor of four and required 15 hours of CPU time on an ALLIANT mini-supercomputer. The small strain elastoplastic computations required 17 hours of CPU time per loading step on an ALLIANT mini-supercomputer. The large strain elastoplastic computations required 0.4 hours of CPU time per loading step on a CRAY supercomputer.

3. ELASTIC ANALYSIS

In the small strain formulation, Hooke's law was implemented

$$\sigma_{ij} = \frac{E}{1+\nu}\left[\delta_{ik}\delta_{jl} + \frac{\nu}{1-2\nu}\delta_{ij}\delta_{kl}\right]\varepsilon_{kl}, \tag{6}$$

where in ordinary notation σ_{ij} is the Cauchy stress, E (>0) is the Young's modulus, $\nu(-1 < \nu < 0.5)$ is the Poisson's ratio, and δ_{ij} is the Kronecker's identity tensor. The small strain tensor ε_{kl} is connected with the displacements u_i as

$$\varepsilon_{ij} = (\partial u_i/\partial X_j + \partial u_j/\partial X_i)/2. \tag{7}$$

The Latin indices range from 1 to 3, repeated indices imply summation in the same range, and the partial differentiation is with respect to the reference fixed Cartesian system X_i.

In the hypoelastic formulation, the constitutive law that was integrated was

$$\mathring{\tau}_{ij} = \frac{E}{1+\nu}\left[\delta_{ik}\delta_{jl} + \frac{\nu}{1-2\nu}\delta_{ij}\delta_{kl}\right]D_{kl}, \tag{8}$$

where $\mathring{\tau}_{ij}$ is the co-rotational (Jaumann) rate of the Kirchhoff stress τ_{ij}, which is related to its total rate $\dot{\tau}_{ij}$ by the spin tensor Ω_{ij} as

$$\mathring{\tau}_{ij} = \dot{\tau}_{ij} - (\Omega_{ik}\tau_{kj} + \tau_{il}\Omega_{lj}) \tag{9}$$

and

$$\Omega_{ij} = (\partial \dot{u}_i/\partial x_j - \partial \dot{u}_j/\partial x_i)/2; \tag{10}$$

$\dot{u}_i$ is the material velocity (or the total rate with respect to any monotonically increasing parameter), and x_i is the current position of a material point initially at X_i. The deformation mapping is $x_i = X_i + u_i$. Finally, D_{ij} is the rate of deformation defined as

$$D_{ij} = (\partial \dot{u}_i/\partial x_j + \partial \dot{u}_j/\partial x_i)/2. \tag{11}$$

The Kirchhoff stress is related to the Cauchy stress through $\tau_{ij} = J\sigma_{ij}$, where J is the determinant of the deformation gradient $(\partial x_i/\partial X_j)$. Note that $J > 0$ is the condition of impenetrability of matter.

In the absence of body and inertia forces, the equilibrium equations that have to be satisfied in the entire body are

$$\partial\sigma_{ij}/\partial x_j = 0. \tag{12}$$

It must be mentioned that the hypoelastic eqn (8) is only approximately derivable from a work potential to within terms of stress divided by the elastic modulus in comparison to unity. Furthermore, integration of eqn (8) may lead to stress oscillations, in particular for shear strains larger than unity (Nagtegaal and de Jong, 1982). In the present calculations, the shear strains were found to be less than unity (of the order 0.5 for $\nu = 0.3$), apart from the region near the indenter's tip. The principal stresses were nearly proportional and thus almost coaxial with the principal strains. No oscillatory behavior of the hypoelastic solution was detected, the imposed rotations from the indenter's inclined planes being small [22°; Fig. 1(b)]. That would not have been the case, had the indenter been very sharp [indenter's angle less than 110°; Fig. 1(b)]. Obviously, a hyperelastic formulation could have been more consistent in treating large strains, however, also due to lack of knowledge of the hyperelastic potentials of the elastoplastic materials to be examined in sequence, such analysis was discarded at present. Using the same elastic constants, the small strain and the hypoelastic formulation gave similar bulk and field results; some of the results for the large strain solution will be presented and discussed in the following analysis.

The total load P, applied in one and also in several steps, was related to the indentation depth h, of the indenter's tip [Fig. 1(b)]. The indentation depth is the only characteristic length of the problem. Therefore, from dimensional considerations, the average contact pressure must be constant. With this in mind, the geometry of the problem indicates a parabolic relation between total load and indentation depth. Indeed, a parabolic relation was numerically found, within 1.0% accuracy, following the explicit form

$$P = 2.0746(1-0.1655\nu-0.1737\nu^2-0.1862\nu^3)\frac{E}{1-\nu^2}h^2, \tag{13}$$

where the constant $E/(1-\nu^2)$ was introduced for comparison with the known cone and circular punch elastic indentation results. As seen in eqn (13), the total load depends very weakly on the Poisson's ratio, which was found by curve fitting of results where ν varied between -0.5 and 0.45. The large strain hypoelastic analysis gave 0.1% increased values of P, as compared with the small strain analysis [eqn (13)] and the same P–h relation for loading and unloading.

The projected indented area was found to deviate from a square, as indicated in Figs 3 and 4. Therefore, superposition of the square punch solution in the spirit of Sneddon (1965) may be questionable in this case. The average contact pressure, p_{av}, is defined as the ratio of the applied load divided by the true projected contact area (i.e. computed contact area as viewed from the surface). Within 4.7% accuracy, it was found numerically that the average contact pressure is constant (load independent) and is related to the elastic properties as

$$p_{av} = 0.2108(1-0.1655\nu-0.1737\nu^2-0.1862\nu^3)\frac{E}{1-\nu^2}. \tag{14}$$

Obviously, the contact area scales with h^2. If the average contact pressure is defined as load per unit of true contact area $\bar{p}_{av}$, then from Fig. 1(b)

$$\bar{p}_{av} = p_{av}/\cos(22°). \tag{15}$$

The formulae (13) and (14) resemble the corresponding forms for a conical (Rockwell) indenter of half apical angle θ derived by Sneddon (1965); $P = 2\tan\theta Eh^2/(\pi(1-\nu^2))$, $p_{av} = \cot\theta E/(2(1-\nu^2))$. It should be noted that it is not possible to find total agreement between the Rockwell and the Vickers elastic solution; fixing the apical angle to have good agreement between average contact pressure leads to substantial difference (16%) in the load–depth relation and vice versa. In a recent work, Bilodeau (1992) reports for the

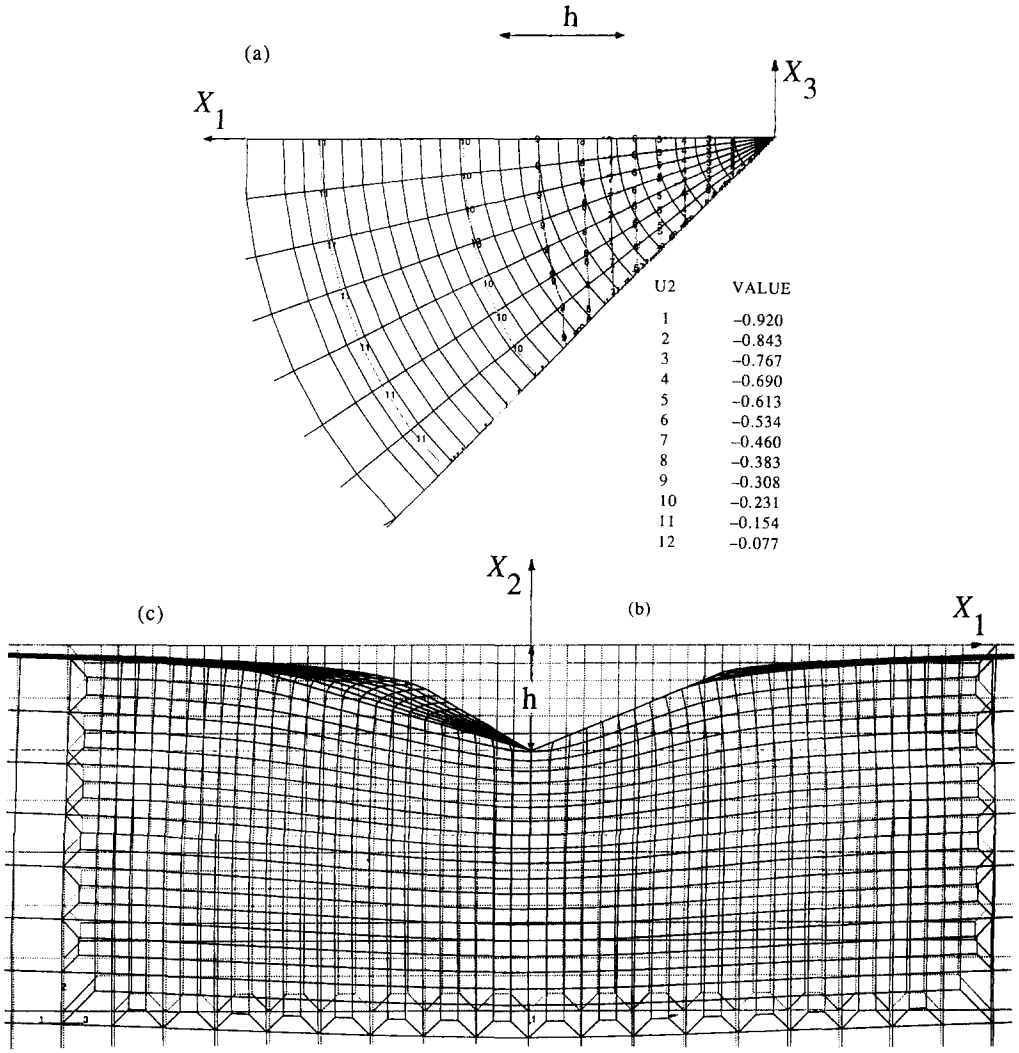

Fig. 3. The deformation pattern close to the indented area for a linear elastic, isotropic material (small strain analysis); (a) normalized vertical deformation u_2/h, viewed from the surface (side I), (b) view from X_1X_2 plane (side II), (c) view from side III. Deformation and coordinates scale with indentation depth h. $\nu = 0.3$.

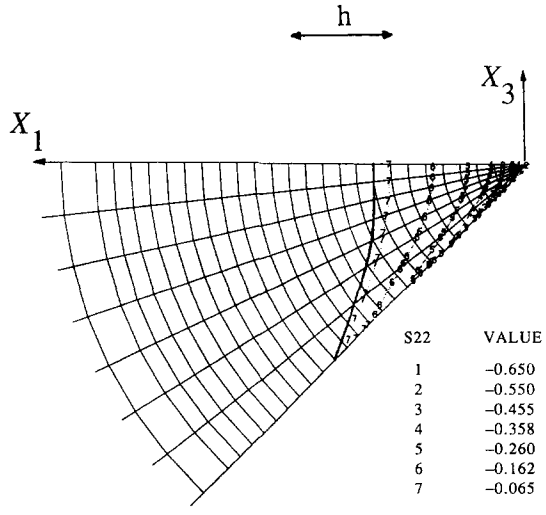

Fig. 4. Normal contact forces per unit of reference surface (S_{22}) for the elastic case, for indentation deformation given in Fig. 3. The projected contact area is also shown. The tractions are normalized by $E/(1-\nu^2)$. The indentation depth h is also shown. $\nu = 0.3$.

Vickers small strain elastic analysis a constant of $0.74563/\tan(\pi/2-\theta)$ for the force (13), and a constant $0.4982\tan(\pi/2-\theta)$ for the average contact pressure (14). For the Vickers test, with $\theta = 68°$, the present results are in 4.4% (for P) and 2.7% (for p_{av}) error with Bilodeau's approximations for $\nu = 0.3$; the reason is that the true contact area was not accounted for (as we will see in the following, the true projected contact area is not a square).

As expected, the deformation was found to scale directly with the indentation depth h, and the deformed mesh is shown in Fig. 3 for $\nu = 0.3$. Note the substantial sinking-in of material, $0.25 \div 0.41h$ at the contact perimeter, as shown in Figs 3(b,c). Material sinking-in will be discussed further in the strain hardening elastoplastic analysis section. Such effect will also be encountered in the linear strain hardening elastoplastic analysis to follow. In-plane slipping was found at the contact area, which was not in a monotonic outward direction. At the contact region, the tangential displacements were very small compared to the vertical ones, except very close to the tip of the indenter, partly justifying the frictionless assumption (further investigation on friction is in progress).

The normal contact forces per unit of reference surface are shown in Fig. 4 for $\nu = 0.3$. These are essentially second Piola–Kirchhoff tractions S_{22}, and scale with p_{av}. In Fig. 4, the development of a singularity of the contact tractions at the indenter's tip can be observed. The singularity of the contact tractions is an integrable singularity; the integration of the surface tractions over the contact area gives the applied force. Milder stress concentrations occur at the sharp edges [imprint diagonals in Fig. 1(a)] of the indenter. Examining the regularity of the numerical solution, it was found that the contact tractions form a logarithmic singularity at the indenter's tip, as it is approached in the radial direction, in agreement with the conical indentation result. The nature of the contact stress singularity at the indentation edges, as they are approached in the circumferential direction, was found to be logarithmic, however, within less accuracy than in the radial direction. On the surface $X_2 = 0$, denote by (r, ϕ) the polar coordinates where $r^2 = X_1^2 + X_3^2$ and $\tan\phi = X_3/X_1$. It was found numerically, within 6.2% accuracy, that the contact tractions can be asymptotically approximated as ($\nu = 0.3$)

$$S_{22}(1-\nu^2)/E = -1.269\ln(r/h)\ln(\phi+\pi/4); \quad r \to 0, \quad \phi \to -\pi/4, \tag{16}$$

with a range of validity $r < h/2$, $-\pi/4 < \phi < -6\pi/28$. The functional form of eqn (16) is suggested by the small strain asymptotic analysis of the sharp contact problem. For $-0.5 < \nu < 0.45$, the projected contact contours were found numerically by curve fitting, within 3% accuracy, to be parts of hyperbolas that follow the relation

$$\frac{(X_1/h)^2}{2.053} - \frac{(X_3/h)^2}{4.863} = 1. \tag{17}$$

Such indentation shapes have been observed in anisotropic fiber reinforced composites indented along the fiber direction (Lesko *et al.*, 1991). Local refinement of the mesh close to the edges did not change the presented results much. For the finite deformation hypoelastic formulation, the stress singularity was confined close to the indenter's tip, but not along its edges. The solution eventually followed the Boussinesq solution of a point force normal to the surface of a semi-infinite, linear elastic, isotropic body, after a distance of about $5h$ from the indentation tip.

For $\nu = 0.3$, Fig. 5 shows the isobars of the normalized Mises effective stress, $\sigma_e = (\frac{3}{2}\sigma'_{ij}\sigma'_{ij})^{1/2}$, where σ'_{ij} is the deviatoric Cauchy stress $\sigma'_{ij} = \sigma_{ij} - \delta_{ij}\sigma_{kk}/3$. The effective strain is also singular with high values appearing over a substantial part of the contact area. This fact renders the present elastic analysis of little or no direct use for metals and ceramic materials at ambience. Some potential use of the elastic solution may be in relation to viscoelastic materials (initial response). For comparison, the corresponding isobars of the normalized Mises stress for the large strain hypoelastic solution for the same indentation depth are shown in Fig. 6. It is clear that the small strain results in Fig. 5 are essentially

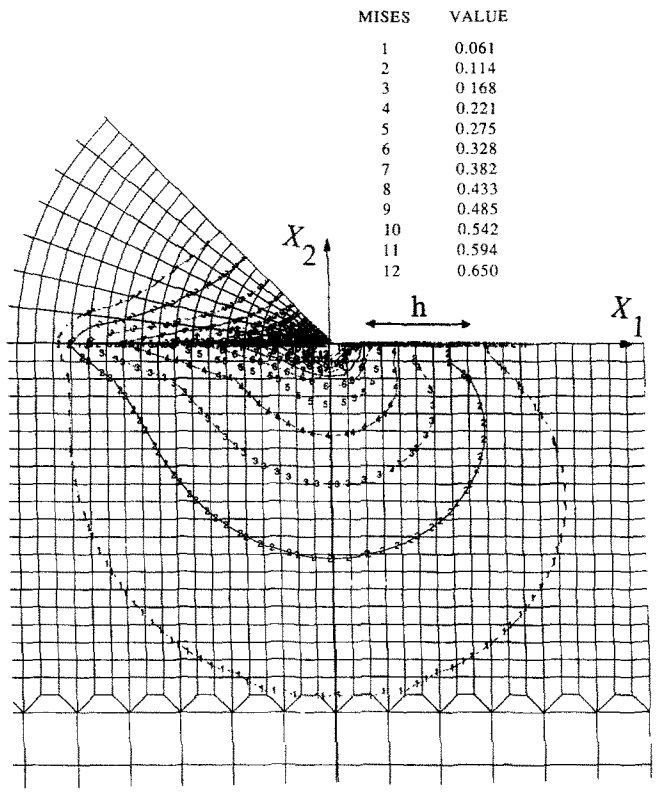

Fig. 5. Mises effective stress (σ_e) for the small strain elastic case (see Fig. 3 for the deformation). The stresses are normalized by $E/(1-\nu^2)$. The indentation depth h is also shown. $\nu = 0.3$.

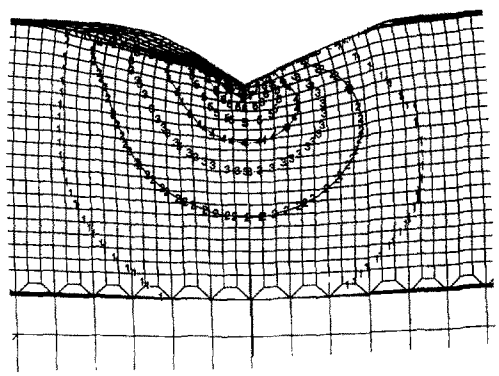

Fig. 6. Mises effective stress (σ_e) for the large strain hypoelastic case. The Cauchy stress levels are as for the small strain calculations (Fig. 5). The indentation depth h is as for the small strain analysis (Fig. 5). $\nu = 0.3$.

mapped on the deformed configuration in Fig. 6. It is interesting to examine the singularity of the Cauchy stresses in the deformed configuration. Following Williams (1952), the stress singularity along the indentation edges, for the particular case of the Vickers indenter (dihedral angle 149.29°), is $r^{-0.252}$ where r is the radial distance from the edge in the deformed configuration. Asymptotic numerical analysis gave a stress singularity of $r^{-0.260}$, however, with a very small range of validity $0 < r < h/2$. For larger radius the stress singularity was found to be $r^{-0.4}$, and further away it approached the Boussinesq solution r^{-2}.

In Fig. 7, the isobars of the normalized hydrostatic stress $p = \sigma_{kk}/3$, are plotted for $\nu = 0.3$. Note that the hydrostatic and the Mises stress fields are highly asymmetrical with respect to the loading direction but tend, as expected, to the Boussinesq point force solution away from the contact area.

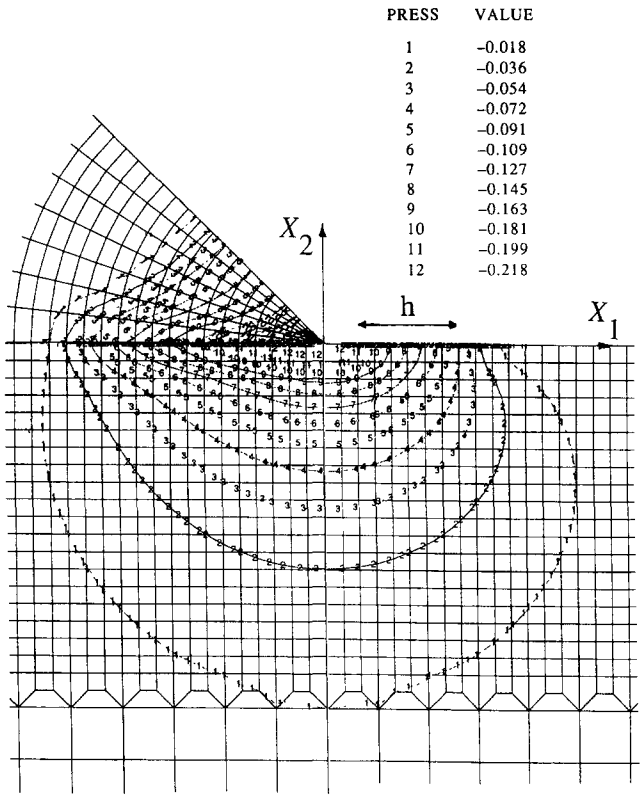

Fig. 7. Hydrostatic stress (p) for the small strain elastic case (see Fig. 3 for the deformation). The stresses are normalized by $E/(1-\nu^2)$. The indentation depth h is also shown. $\nu = 0.3$.

Due to the homogeneous strain energy density, the small strain elastic problem is self similar, the coordinates and displacements can be normalized by the indentation depth h, and the stresses by p_{av}. The normalized results are then universal with small dependence on the Poisson's ratio. The hypoelastic solution also gave self similar results. The hypoelastic solution gave Cauchy stresses which are almost identical to those obtained by the small strain analysis with same elastic constants, apart from a region very close to the indenter's edges at which the stresses were much smaller compared to the small strain analysis.

Finally, it must be mentioned that all the principal stresses were found to be compressive. Thus, if indentation induced crack analysis is to be attempted with the present elastic solution, the necessary result is that cracks initiate symmetrically from the indentation tip due to high shear stresses and extend preferably along the indenter's diagonal edges. This observation may be of interest for investigating indentation induced cracks in hard brittle materials such as ceramics and glasses using the present elastic results.

4. ELASTOPLASTIC ANALYSIS

In reality is is very difficult to make a purely elastic indentation; except for rubbers, foams etc., the materials will deform irreversibly and/or crack. Many important engineering metals at low temperatures can be modeled as incrementally elastoplastic, isothermal, rate independent materials with isotropic strain hardening. This type of model will be used in this section.

The problem is analysed within small and large strain formulation. For the small strain formulation, the Prandtl–Reuss equations to be integrated are

$$\dot{\sigma}_{ij} = \frac{E}{1+\nu}\left(\delta_{ik}\delta_{jl} + \frac{\nu}{1-2\nu}\delta_{ij}\delta_{kl} - \frac{3\sigma'_{ij}\sigma'_{kl}E/(1+\nu)}{2\sigma_e^2\left(\frac{2}{3}H + \frac{E}{1+\nu}\right)}\right)\dot{\varepsilon}_{kl}. \tag{18}$$

In eqn (18), $H\ (=\mathrm{d}\sigma/\mathrm{d}\varepsilon_p)$ is the instantaneous slope of the uniaxial nominal stress, σ, versus

the engineering (nominal) plastic strain, $\varepsilon_p = \varepsilon - \sigma/E$, given from a simple uniaxial tension test [$\sigma = \sigma(\varepsilon)$]. The dot superscript indicates time variation. Additive decomposition of the total strain rate in an elastic and a plastic part is assumed in the usual way. The accumulation of total plastic strain is measured from the line integral of the plastic strain rates, $\dot{\varepsilon}^p_{ij}$ (p is not a free index),

$$\varepsilon_p = \int_0^t (\tfrac{2}{3}\dot{\varepsilon}^p_{ij}\dot{\varepsilon}^p_{ij})^{1/2}\,dt. \tag{19}$$

Equation (18) applies for plastic loading where the Mises effective stress is $\sigma_e = \sigma(\varepsilon_p)$. The initial yield stress is $\sigma_y = \sigma(\varepsilon_p = 0)$. For elastic loading or unloading, eqn (6) holds.

For the large strain formulation, the Prandtl–Reuss equations to be integrated are

$$\mathring{\tau}_{ij} = \frac{E}{1+\nu}\left(\delta_{ik}\delta_{jl} + \frac{\nu}{1-2\nu}\delta_{ij}\delta_{kl} - \frac{3\tau'_{ij}\tau'_{kl}E/(1+\nu)}{2\tau_e^2\left(\frac{2}{3}H + \frac{E}{1+\nu}\right)}\right)D_{kl}. \tag{20}$$

In eqn (20), H ($=d\tau/d\varepsilon_{lp}$) is the instantaneous slope of the uniaxial tensile Kirchhoff stress τ, versus the logarithmic plastic strain ε_{lp} (l, p are not free indices). The effective stress is $\tau_e = (\frac{3}{2}\tau'_{ij}\tau'_{ij})$, where τ'_{ij} is the deviatoric part of the Kirchhoff stress. Additive decomposition of the total deformation rate in an elastic and a plastic part is assumed. The accumulation of plastic strain ε_{lp}, is measured from the line integral of the plastic part of the deformation rate D^p_{ij}, [see also eqn (19)]. Equation (20) applies for the plastic loading where the effective stress is $\tau_e = \tau(\varepsilon_{lp})$. The yield stress $\tau_y = \tau(\varepsilon_{lp} = 0)$. For the elastic loading or unloading, eqn (8) holds. The elastoplastic relations (20) apply reasonably well for low strain hardening (small values of H/E) in which case the elastic strains are much smaller than the plastic ones (Needleman, 1972). Mainly stable material behavior ($0 < H/E < 1$) was examined, but some results pertinent to elastic–perfectly plastic ($H/E = 0$) materials will also be presented. The constitutive law is homogeneous (elastoplastic properties independent of X_i). No initial stresses (e.g. residual stresses) were assumed in the present calculations.

A linearized incremental contact formulation can be stated as

$$\Delta u_i = \dot{u}_i \Delta t, \quad N_i \Delta u_i \leqslant N_1 x_1 + N_3 x_3 - hN_2 \quad \text{on} \quad \Gamma_c, \tag{21}$$

where Γ_c is the possible contact surface of the current deformed half space Φ. N_i is the unit vector inward normal to the rigid surface (Fig. 1), Δt is an arbitrarily small time increment and $h \geqslant 0$ is the current indentation depth prescribed by the loading.

Define the sub-Hilbert space of displacements v_i

$$V = \{v_i \in H^1(\Phi) | v_i \to 0, |x_i \to \infty\}, \tag{22}$$

and its cone

$$K = \{(v_i \in V | N_i \Delta v_i \leqslant N_1 x_1 + N_3 x_3 - hN_2 \quad \text{on} \quad \Gamma_c\}. \tag{23}$$

The Signorini rigid punch problem for large deformation elasticity gives the following variational inequality defined in the current deformed configuration: find $\Delta u_i \in K$ and $\Delta h \in R^+$ such that $\forall v_i \in K$: $v_2 - \Delta u_2 \leqslant h - \Delta h$, and $\sigma_{1j}N_j = \sigma_{3j}N_j = 0$, $\sigma_{2j}N_j \leqslant 0$ on Γ_c ($\sigma_{2j}N_j = 0$ at the boundary of Γ_c). Equivalently,

$$\int_{\Phi} \Delta\sigma_{ij} E_{ij}(v-\Delta u)\,\mathrm{d}\Phi + \int_{\Phi} \left(\sigma_{ki}E_{kj}(\Delta u)+\sigma_{kj}E_{ki}(\Delta u)-\sigma_{jk}\frac{\partial}{\partial x_k}\Delta u_i\right) \times \left(\frac{\partial v_i}{\partial x_j}-\frac{\partial}{\partial x_j}\Delta u_i\right)\mathrm{d}\Phi \geqslant -P(h-\Delta h), \quad (24)$$

where

$$E_{ij}(v) = \left(\frac{\partial v_i}{\partial x_j}+\frac{\partial v_j}{\partial x_i}\right)\Big/2, \quad (25)$$

and $\Delta\sigma_{ij}$ is the change of the Cauchy stress due to Δu_i. Plasticity is incorporated by using the current elastoplastic moduli to compute $\Delta\sigma_{ij}$. This linearized incremental contact problem (24) can be solved with the same penalty method as for the linear small strain elastic contact problem [i.e. eqn (1)]. For stable material response, as in the present, the solution of eqn (24) exists and is unique (Kikuchi and Oden, 1988). The total load applied to the indenter is

$$P = -\int_{\Gamma_c} \sigma_{2j} N_j \,\mathrm{d}\Gamma_c. \quad (26)$$

We simulated the Vickers punch on aluminium 7075-T6 and 6061-T6. These materials are well characterized and are very important because they are extensively used in airspace and automotive structural parts. They exhibit very little strain rate effect. The fineness of their microstructure is suitable for microindentation experiments. Their nominal uniaxial compression response was modeled after the experimental results of Maiden and Green (1966). The uniaxial nominal compression stress versus nominal plastic strain curves were implemented by piecewise linear interpolation of the experimental points shown in Figs 8(a,b). The elastic modulus of 7075-T6 was 72 GPa, and that of 6061-T6 was 70 GPa. Poisson's ratio was 0.28, the same for both materials. The yield stress σ_y of 7075-T6 and 6061-T6 was 415.7 MPa and 287.4 MPa, respectively. For the large strain elastoplastic analysis, the nominal uniaxial compression curves were translated to true tensile stress versus logarithmic strain tension curves by using the relations $\tau = \sigma(1-\varepsilon_p)$ and $\varepsilon_{lp} = -\ln(1-\varepsilon_p)$. It was found from the elastic analysis (see previous section) that large strains develop that are unattainable from the experimental uniaxial compression tests. In view of the scope of the present analysis, the experimental results were extrapolated in different ways, as shown in Fig. 8(c). When no hardening was considered, the maximum stress in uniaxial compression, σ_u, was taken as 669.8 MPa and 388.6 MPa for 7075-T6 and 6061-T6, respectively. In addition, we solved the elastic–perfectly plastic response with Young's modulus 18.6 GPa, Poisson's ratio 0.35, and yield stress 317.6 MPa. The plastic constitutive input corresponds to tantalum.

The typical mesh used in the elastoplastic case is shown in Fig. 9 (7350 eight-noded elements, 7988 nodes). Figures of the deformation and stress fields are shown for aluminium 7075-T6. Similar figures were found for aluminium 6061-T6 and tantalum. First we present the analysis and results for no hardening with the small strain formulation. Then, we present the analysis for linear strain hardening at large strains ($>3\%$) with small and large strain formulation.

4.1. *No hardening case*

The two most important features given by an indentation test is the load–indentation depth relation and the hardness (that is the average contact pressure). Until now, universal formulae for these quantities at Vickers indentation have not been presented in the literature. This is in contrast to the situation for Brinell indentation where the well known Tabor formula is widely accepted as very accurate and in fact has been given a solid theoretical

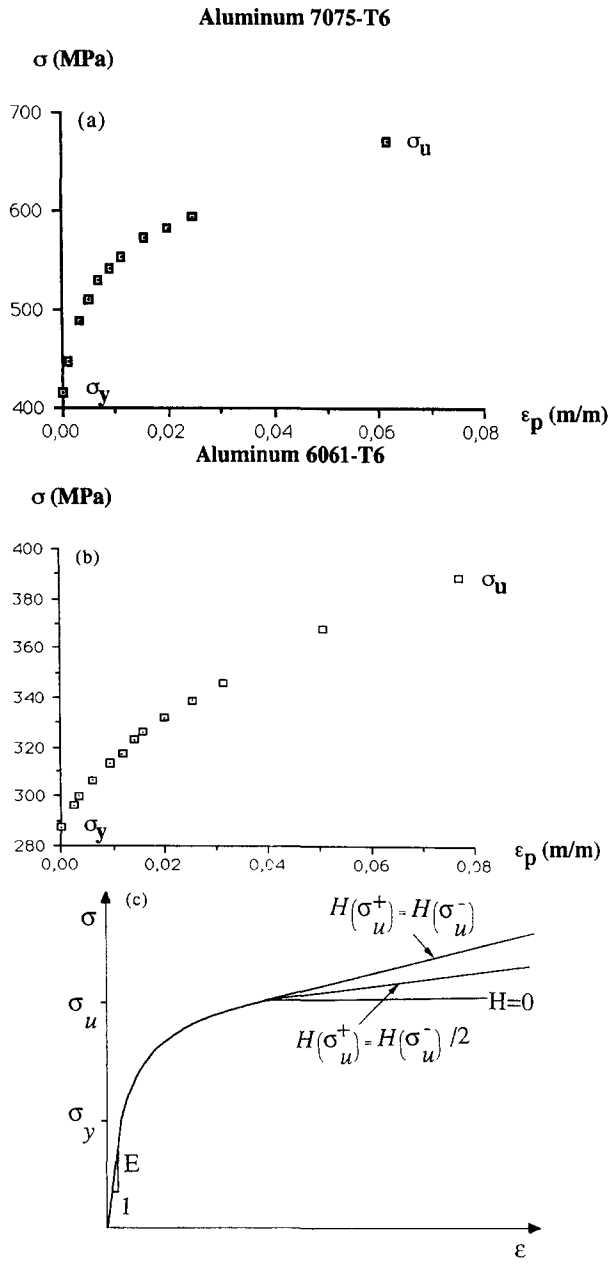

Fig. 8. Uniaxial nominal compression stress versus nominal plastic strain by Maiden and Green (1966); (a) aluminium 7075-T6, (b) aluminium 6061-T6, (c) schematic of the assumed compressive strain hardening, extrapolating Figs 7(a,b) for large strains.

background by Hill *et al.* (1989). Johnson (1970), however, made an attempt to use results from cone indentation of elastoplastic strain hardening materials in order to find a universal formula for the Vickers hardness through the relation

$$p_{av} = \tfrac{2}{3}\sigma_r\left(1+\ln\frac{E\tan\psi}{3\sigma_y}\right). \tag{27}$$

In eqn (27), σ_r is the flow stress in uniaxial compression at a plastic equivalent strain of 0.07 [this was Johnson's choice; originally Tabor (1951) suggested an equivalent strain of 0.08] and the angle ψ was chosen to be 19.7° in order to get the same volume of material displaced at cone indentation as much as at the Vickers indentation.

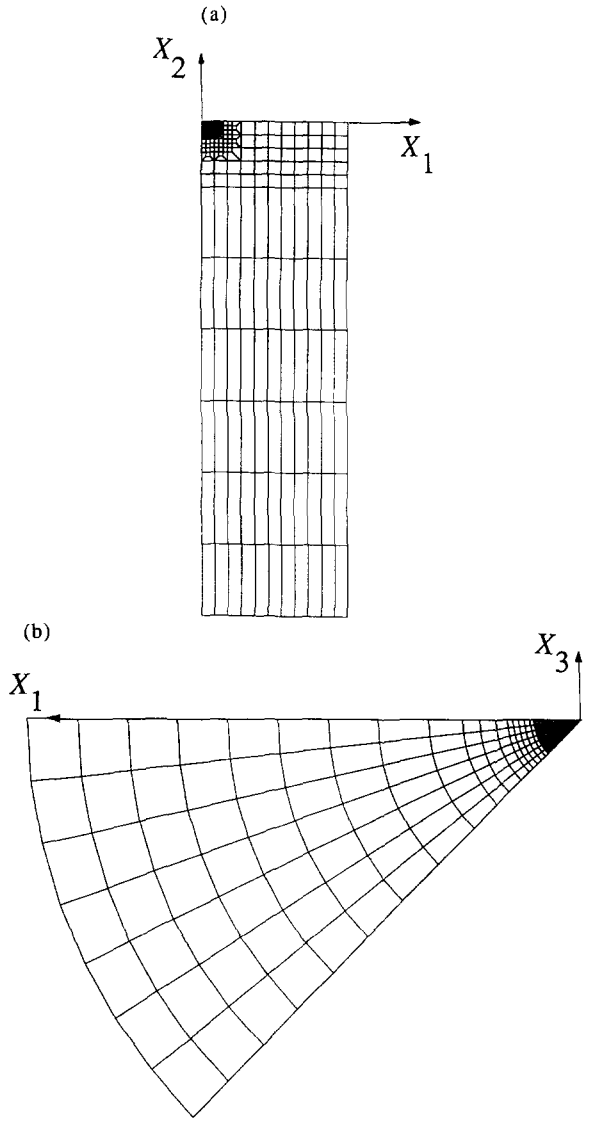

Fig. 9. The FEM mesh used mainly in the elastoplastic analysis of the Vickers indentation; (a) view from X_1X_2 plane (side II), (b) view from the surface (side I). 7350 eight-noded elements (7988 nodes).

When comparing the results from eqn (27) with our numerical results, we found very good agreement when materials with constant strain hardening were considered. However, eqn (27) could not completely capture the influence of the yield stress and the pile-up (or sinking-in) of material on the average pressure, as well as the influence of different types of strain hardening at large strains. Therefore, as a first attempt we assumed that the influence of the yield stress and pile-up could be described up to first order through a series expansion resulting in the relation for the average contact pressure (load divided by the true projected contact area)

$$p_{av} = C\sigma_u(1+\sigma_y/\sigma_u)\left(1+\ln\frac{E\tan 22^\circ}{3\sigma_y}\right)\left(1-\frac{u_{2max}}{h}\right), \tag{28}$$

where, in the spirit of Tabor (1951), we chose the angle ψ in eqn (27) to be 22°, the actual indentation angle of Vickers indentation. u_{2max} is the maximum (positive) surface displacement due to material pile-up (6.7% of h for tantalum, 10.7% of h for 6061-T6, 8.2% of h for 7075-T6) and that $p_{av} > 0$.

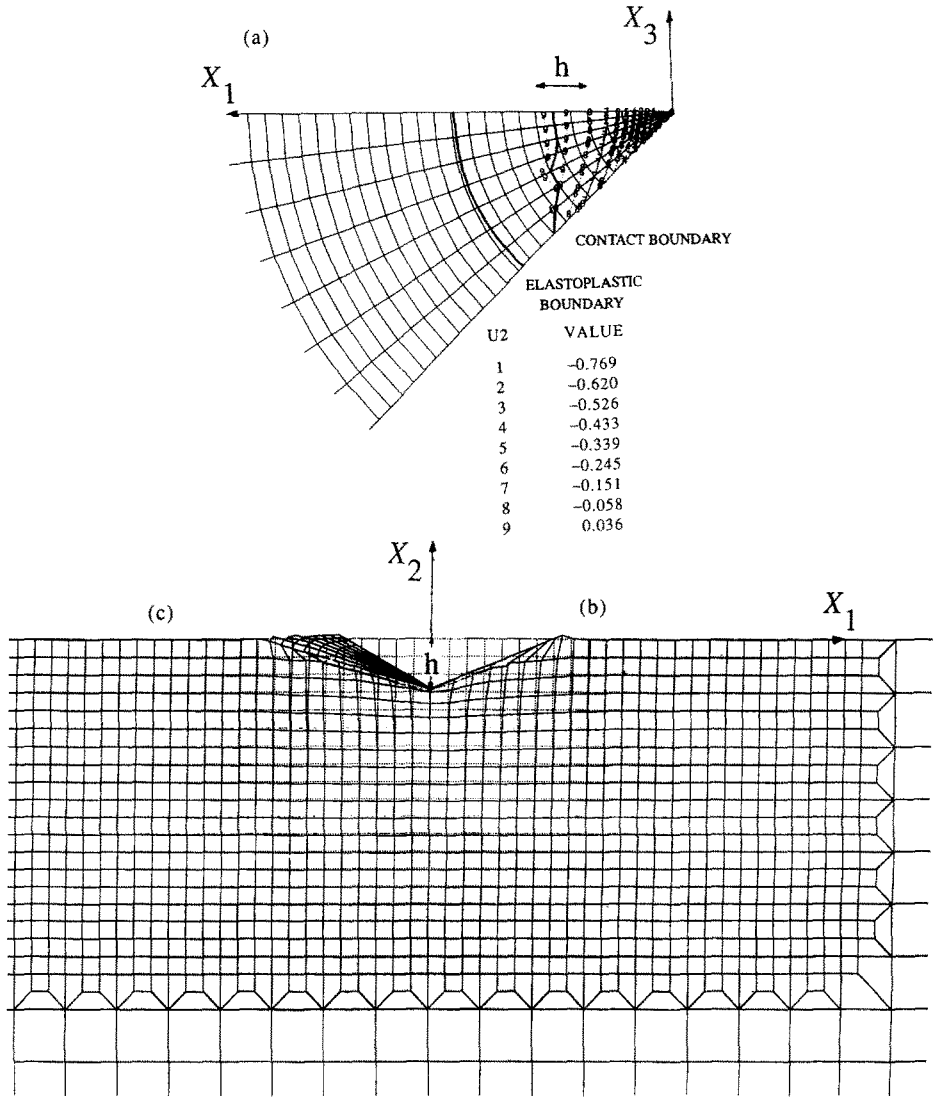

Fig. 10. The deformation pattern at maximum loading of aluminium 7075-T6 (no strain hardening, small strain analysis); (a) normalized vertical deformation u_2/h, contact area and elastoplastic boundary as viewed from the surface (side I), (b) view from X_1X_2 plane (side II), (c) view from side III. Indentation depth h is also shown.

When only elastic–plastic materials or materials with a well defined ultimate stress σ_u were considered, the constant C was determined to be 0.265 and all the small strain numerical results then fell to within 2% error of the ones derived through eqn (28). The formula was found to be insensitive to Poisson's ratio. The influence of σ_u/σ_y was further investigated and it was found that eqn (27) is valid for $1 \leqslant \sigma_u/\sigma_y \leqslant 1.6$, with $\sigma_u = \sigma_y$ for the elastic–perfectly plastic case (we did not carry out calculations for higher σ_u/σ_y values). If the average contact pressure is defined as load per unit of true contact area, then eqn (28) can be used together with eqn (15).

The projected contact area was found to slightly deviate from a square [Fig. 10(a)], whereas in the pure elastic case this was not so (Fig. 4). An interesting feature of the elastic–plastic results, in the absence of strain hardening at large strains, is the uneven piling-up of the material at the edge of the contact contour resulting from plastic incompressibility. This was expected because of the different degree of constraint induced by the indenter's shape. In eqn (28) the correction term $1 - u_{2max}/h$ is due to the piling-up of material (Fig. 10) at the contact contour. The closest correlation with the numerical results was found, if u_{2max} was measured along the X_1-axis. In short, this is a first order approximation of the contact area at piling-up of material. In the case of the contact area being on a perfect square

pyramid, the pointwise correction term would be, within a first order approximation, $1-2(u_2/h)$ where u_2 is the vertical displacement at the contact contour. This quantity, however, is not measurable during the course of an experiment and in view that the contact contour was found to be close to a plane square we used the correction term $1-u_{2\max}/h$ in eqn (28). This choice proved to give excellent agreement with the numerical results and has the advantage of being relatively easy to measure experimentally.

With the formula for p_{av} now determined, the load–indentation depth relation is actually given through simple geometrical considerations as

$$P = 1.06h^2(\tan 22^\circ)^{-2}\sigma_u\left(1+\frac{\sigma_y}{\sigma_u}\right)\left(1+\ln\frac{E\tan 22^\circ}{3\sigma_y}\right)$$

$$= p_{av}4h^2(\tan 22^\circ)^{-2}\left(1-\frac{u_{2\max}}{h}\right)^{-1}, \tag{29}$$

and the numerical results then fall within 5% of the ones given by eqn (29).

It should be emphasized that eqns (28) and (29) were found to be essentially true for cases where the yield stress is defined as the point where the uniaxial compressive stress–strain curve changes abruptly. Furthermore, as mentioned earlier, our numerical calculations show that, in contrast to what is predicted by eqn (27), the average pressure is influenced substantially by the hardening present at high strains (>0.07). As the strain hardening also affects the mode of deformation (sinking-in instead of pile-up) at the contact contour, this feature has to be implemented into eqns (28) and (29), a matter that will be discussed further in Section 4.2.

Some indentation size effect [higher average contact pressure than its steady state value given by eqn (28)] was found for the initial stage of the analysis at low load ($P < 0.18Eh^2$). Hardness experiments also show similar size effect. However, the present results, although tentative, were inconclusive about this issue. Low resolution of contact at low loads (four to five elements) precluded finding accurate estimates for the level of load that is needed for obtaining steady state results. We believe that the explanation of the experimentally observed indentation size effect at low loads cannot be fully addressed with the present level of modeling. Note that at high loads the steady state average contact pressure for the Vickers indentation of elastoplastic materials was found (in accordance with experimental results) approximately independent of the indentation depth, contrary to the Brinell indentation which depends on it. Therefore, the Vickers test may be a more useful and general material test for certain applications where severe constraints on the magnitude of the indentation depth are in place (e.g. microelectronics, nanocomposites, etc.).

The slope, dP/dh, of the load–indentation depth (P–h) curve at the beginning of the unloading is frequently used by experimentalists as input to the circular punch elastic results of Sneddon (1945) when determining the elastic parameters of the indented materials. In view of the present findings on the square shape of the contact area [Fig. 10(a)], a 2% better accuracy can be achieved by using the results derived for a square punch indenting a homogeneous elastic half space (King, 1987). The slope dP/dh is then related to the elastic parameters as

$$\frac{E}{1-\nu^2} = \frac{1}{1.142\sqrt{A_{\max}}}\frac{dP}{dh}, \tag{30}$$

where $A_{\max}$ is the true projected contact area at the end of the loading (maximum applied force at the indenter). The stiffness, dP/dh, was calculated from the initial part of the unloading P–h curve and eqn (30) was found to underestimate the assumed $E/(1-\nu^2)$ value of the 7075-T6 aluminium by less than 5%. Even better results were found for 6061-T6 aluminium and tantalum, the difference being -1% and 4%, respectively. Furthermore, as regards the unloading process, the total amount of elastic recovery of the imprint in the vertical direction was about 10% of the total indentation depth. The applied work is mostly

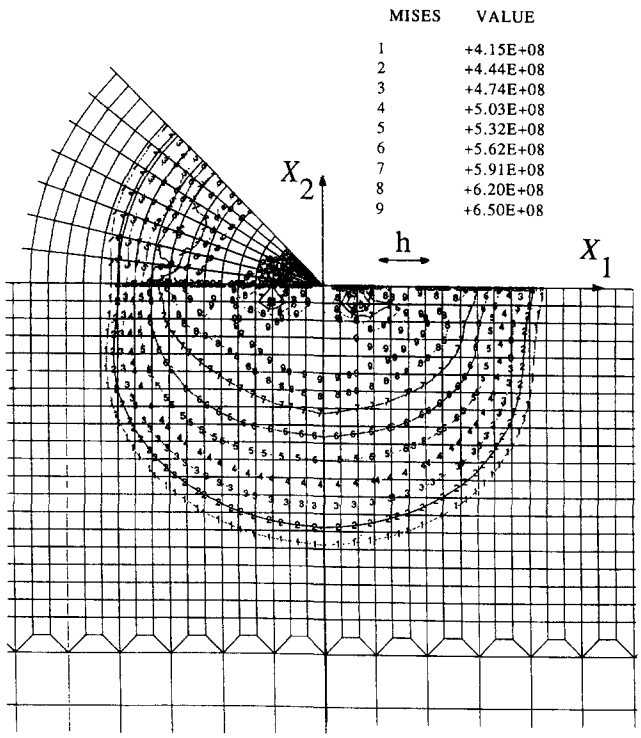

Fig. 11. Steady state Mises effective stress (σ_e) for aluminium 7075-T6 at maximum load (no strain hardening). Units are in Pa. $\sigma_u = 669.8$ MPa, $\sigma_y/E = 0.0058$, $\sigma_u/\sigma_y = 1.6$. The indentation depth h is also shown.

absorbed by a volume of plastically deformed material. However, the imprint projection changed very little upon unloading, a fact that is assuring for the experimental derivation of hardness (maximum applied load divided by the projected residual imprint) and eqn (28) can be used to estimate the hardness from material properties.

The steady state results at maximum load for aluminium 7075-T6 are shown in Figs 10–12; analogous plots for aluminium 6061-T6 and tantalum are very similar. Figure 10 shows the deformation pattern at maximum load which scales with the maximum indentation depth. Due to plastic incompressibility and the indenter's geometric constraint, the material piling-up appears peaking at the contact edge, with absolute maximum along the X_1-axis [its value, $u_{2\max}$, was used in eqn (28)]. This fact is advantageous for the experimental evaluation of hardness because observation of the peaks of the pile-up will unambiguously determine the contact area. Note that the surface displacements approach the initial surface plane from below and the relevant transition region is small. In spite of the low resolution of the piling-up in the present calculations (three to four elements), its peculiar shape appears similar to that computed by Laursen and Simo (1992) for the conical punch.

Figure 11 shows the isobars of the Mises effective stress and also the extent of the plastic region ($\sigma_e = \sigma_y$), that is the elastoplastic boundary at loading. The Mises stress is bounded by σ_u with its maximum at a distance $1.6h$ below the indenter's tip. Local unloading ($0.82\sigma_u$) occurs at the contact surface at a distance $0.8h$ away from the indenter's tip. The elastoplastic boundary extends from the surface approximately twice the imprint diagonal and it appears to be spherical with its center at a depth equal to half the indentation, in partial accordance with the approximation by Johnson (1970). For materials with a well defined ultimate stress σ_u, the radius c of the steady state plastic zone was found to be, within 5% error,

$$c^2 = 0.3P/\sigma_y. \tag{31}$$

For elastic–perfectly plastic materials, Johnson (1970) found $c^2 = 0.63P/\sigma_u$. That result,

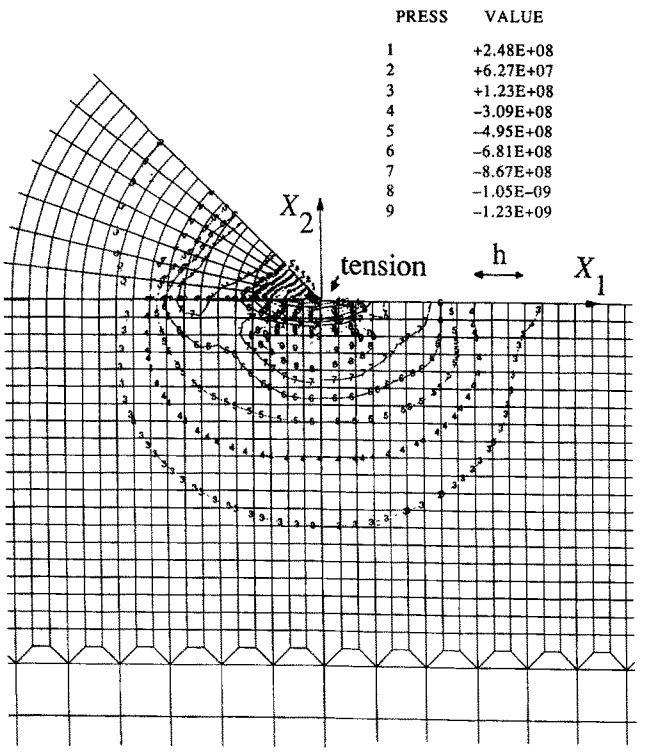

Fig. 12. Steady state hydrostatic stress (p) for aluminium 7075-T6 at maximum load (no strain hardening). Units are in Pa. $\sigma_u = 669.8$ MPa, $\sigma_y/E = 0.0058$, $\sigma_u/\sigma_y = 1.6$. The indentation depth h is also shown.

however, is related to cone indentation and 0.52 instead of 0.63 is suggested for the Vickers indentation. Reformulating eqn (31) as

$$c^2 = 0.3\left(\frac{\sigma_u}{\sigma_y}\right)\frac{P}{\sigma_u}, \tag{32}$$

and using the σ_u/σ_y values of 7075-T6 and 6061-T6, we observe that, within 5%, $c^2 = 0.44P/\sigma_u$ which indicates that the result of Johnson overestimates the plastic region by 18%.

Figure 12 shows the isobars of the hydrostatic stress at maximum load. The hydrostatic stress p shows a clear tensile region that is developed near the indenter's tip. This could be very important in connection to crack formation along the indenter's edges. The maximum tensile hydrostatic stress was $0.37\sigma_u$ at the indenter's tip. The maximum compressive hydrostatic stress was $-1.83\sigma_u$ at a distance h below the indenter's tip.

The contours of the accumulated plastic strain are plotted in Fig. 13. The maximum plastic strain appears at the indenter's tip. No reverse plasticity takes place at unloading. Plastic strain is found to accumulate faster near the contact region (closer to the tip and the sharp edges), in departure from the cone punch solution where plastic strains accumulate concentrically from the indenter's tip. This is in accordance with the Mises stress (Fig. 11) which shows the plastic loading surface emanating from the tip of the indenter and propagating along the contact interface (followed by an unloading regime) and vertically inside the specimen, accumulating plastic strain as shown in Fig. 13.

Figure 14 shows the Mises stress (σ_e) and Fig. 15 shows the hydrostatic stress (p) for aluminium 7075-T6 after complete unloading from steady state at maximum load; analogous plots for aluminium 6061-T6 and tantalum are very similar. Note the different distribution of stresses from the loading case (Figs 11 and 12). For the Mises stress, the highest value ($0.91\sigma_u$) appears at a distance h below the surface along the indentation direction. Another maximum in the Mises stress ($0.79\sigma_u$) appears at the surface, close to

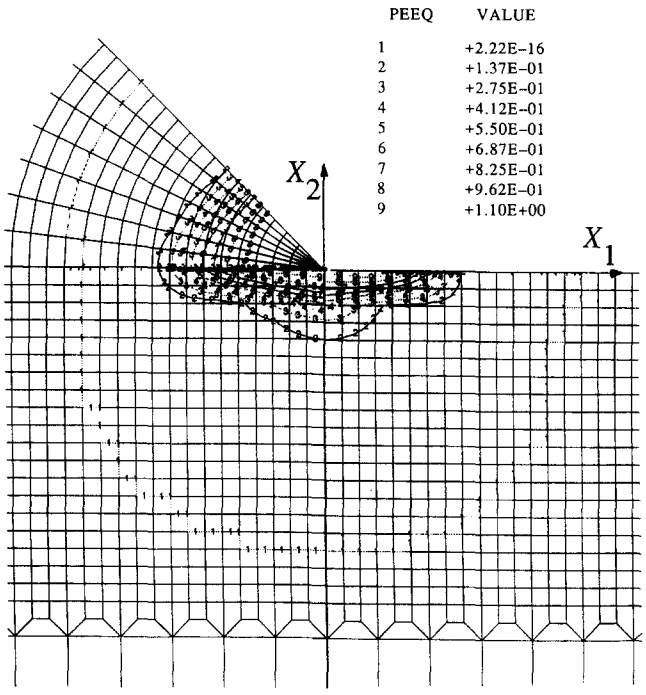

Fig. 13. Steady state accumulated plastic strain for aluminium 7075-T6 (no strain hardening).

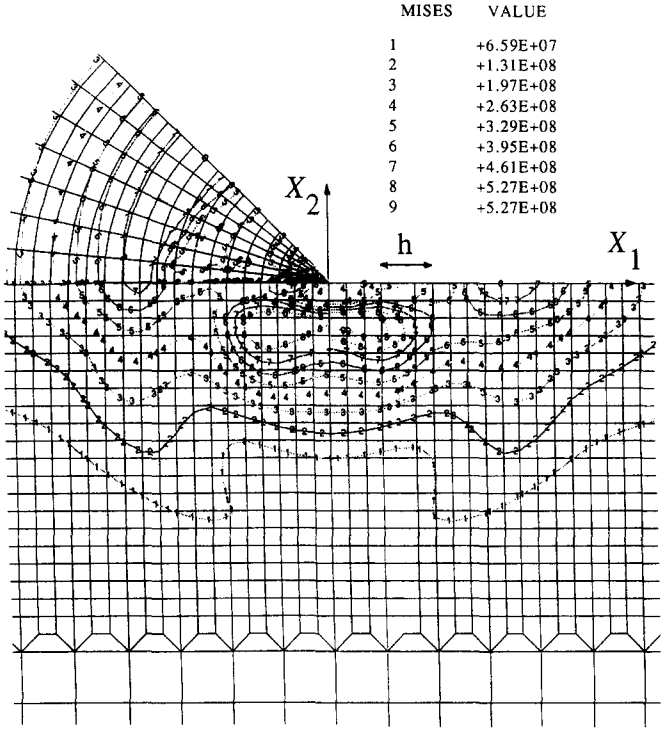

Fig. 14. Mises effective stress (σ_e) for aluminium 7075-T6 after complete unloading from steady state at maximum load (no strain hardening). Units are in Pa. $\sigma_u = 669.8$ MPa, $\sigma_y/E = 0.0058$, $\sigma_u/\sigma_y = 1.6$. The indentation depth h is also shown.

the end of the pile-up, a distance $4h$ from the indenter's tip. The residual hydrostatic stress has a maximum compressive value ($0.74\sigma_u$) at a distance h below the indenter's tip. The residual hydrostatic stress is still positive close to the indenter's tip, even though its explicit tensile values are 2.5 times lower than the corresponding values at loading. The residual

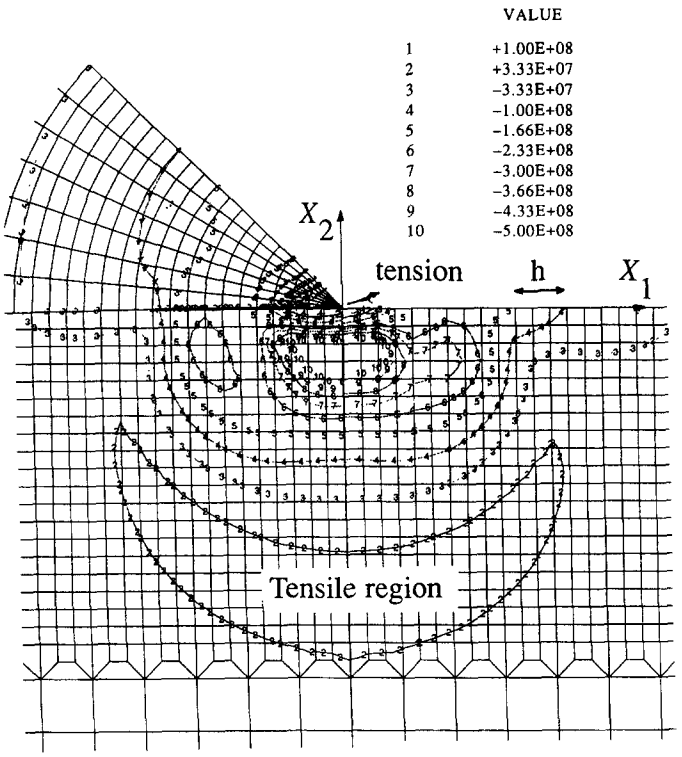

Fig. 15. Hydrostatic stress (p) for aluminium 7075-T6 after complete unloading from steady state at maximum load (no strain hardening). Units are in Pa. $\sigma_u = 669.8$ MPa, $\sigma_y/E = 0.0058$, $\sigma_u/\sigma_y = 1.6$. The indentation depth h is also shown.

hydrostatic stress is also positive ($0.2\sigma_u$) close to the residual plastic boundary. The implication of these observations to crack formation will be discussed below.

Comparing the results of all analysed materials, they were found to be self similar and nearly independent of the Poisson's ratio. The self similarity of the small strain solution is to be expected because of the homogeneous stress–strain relations at zero strain hardening. For a particular choice of σ_y/E, the fields become universal if the coordinates and displacements are normalized by the indentation depth h, and the stresses by p_{av} from eqn (28) at loading (and by E for unloading). The plastic strains need no normalization. Once the steady state results are achieved, increasing load results in higher spacial resolution of the already presented figures of the mechanical fields.

4.2. *Linear hardening case*

Up to this point we have presented results where an ultimate compressive stress σ_u with zero hardening thereafter are assumed for the uniaxial response. In the following we present some results where linear strain hardening was assumed for stresses higher than σ_u. For the sake of generality, a number of different values of strain hardening, H ($=d\sigma/d\varepsilon_p$), was considered as shown in Fig. 8(c) and the results were correlated according to the formulae presented in the previous section. For comparison, the same indentation depth as for the no hardening case was taken. We begin with the results from small strain calculations.

Regarding eqns (29) and (28) governing the applied load and the average contact pressure, it was found that these equations still hold within the reported errors, if the ultimate stress σ_u, is replaced by the stress evaluated at $\varepsilon_p = 0.3$ on the uniaxial compression curve [Fig. 8(c)]. This somewhat surprising result is valid for all the different types of hardening analysed and suggests that there indeed is a representative strain present in the problem, but not the value 0.08 as proposed by Tabor (1951). In the Brinell test, the representative strain is $0.4a/D$, where a is the contact radius and D is the diameter of the indenting rigid sphere. The isocontours of accumulated plastic strain have the same shape as for the no hardening case (Fig. 13), with maximum plastic strain appearing at the

indenter's tip, but about 16% lower than the no hardening case. Close inspection of Fig. 13 reveals that this equivalent plastic strain level of 0.3 corresponds to a change in the shape of the plastic strain distribution.

Hardening had a large influence on the deformation mode at the contact contour. Compared with the no hardening case, the results showed that piling-up of material was substantially reduced, if hardening after σ_u was considered; and if linear hardening with $H(\sigma_u^+) = H(\sigma_u^-)$ was present, sinking-in occurred at the contact boundary contour (note that sinking-in was found in the pure elastic case). The projected contact area was found nearly square with its edges like very shallow hyperbolas (pronounced hyperbolas were found in the pure elastic case, Fig. 4). In this case the area of contact is smaller than what could be expected from purely geometrical considerations. It was, however, not possible to express the effect of sinking-in on the average contact pressure in any experimentally measurable quantity. Still, the derived results indicate that eqn (28) holds also at this situation, if the correction term $1-u_{2\max}/h$ is replaced by 1, and the factor 0.265 is replaced by 0.27 (and accordingly 1.06 is replaced by 1.08 in eqn (29)). Regarding eqn (28), this modification gave an effect of sinking-in of material due to hardening but otherwise independent of material properties. Although definitely an approximation, such a result is not only in good agreement with the present numerical analysis, but also in line with results from earlier analysis of the Brinell indentation (Hill *et al.*, 1989), where it is shown that transition from sinking-in to piling-up is only dependent on the type of plastic hardening and in fact sinking-in only occurs at, or close to, linear hardening (power law hardening $n > 4$). In our case, this would correspond to linear hardening, $H(\sigma_u^+) = H(\sigma_u^-)$ [Fig. 8(c)]. Note that substantial sinking-in was also observed in the pure elastic response [Figs 3(b,c)]. Some further similarities with the purely elastic case will be discussed below.

As regards the radius of the plastic zone c, no direct correlation could be found between the results for materials with a well defined ultimate stress compared to results for materials exhibiting strain hardening. The plastic zone cannot be calculated using eqn (31). However, very good agreement (within 3.5%) was found, if the factor 0.3 in eqn (31) was replaced by 0.48. Surprisingly, this factor proved to be almost constant regardless of the type of plastic hardening and, incidentally, is close to the factor reported by Johnson (1970) for Vickers indentation of elastic–perfectly plastic materials.

The total amount of elastic recovery of the imprint was much larger than that of the elastic–perfectly plastic case, as also indicated by experimental P–h curves. Hardening severely reduced the validity of eqn (30). Sinking-in, found for strain hardening, worsens the approximation of elastic unloading according to a square punch. Therefore, the unloading part of the load–indentation depth (P—h) curve can only be used with confidence for low strain hardening material response. Moreover, sinking-in means problems for the experimental evaluation of hardness, since the true contact area could be uncertain, if relying on mere observation of the residual imprint. This is clearly a disadvantage for the direct experimental evaluation of hardness, as opposed to the piling-up situation encountered in the no hardening case (see previous section). The proposed corrections from the present work can be very useful in this respect.

In Figs 16 and 17, the hydrostatic stress (p) is shown for steady state loading at maximum load and complete unloading respectively for aluminium 7075-T6 when constant plastic hardening, $H(\sigma_u^+) = H(\sigma_u^-)$, is assumed at large compressive strains [Fig. 8(c)]. As can be seen in Fig. 16, no tensile region was found during loading. This was not the case for the no hardening case, as can be shown by comparing Figs 16 and 12. The maximum compressive value ($-3\sigma_u$) appeared at the surface, a distance $2h$ from the indenter's tip. Tensile residual stresses appear close to the indentation tip and away from the imprint (close to the residual plastic boundary) at unloading (Fig. 17). This was also observed for the no hardening case (Fig. 15). The residual tensile hydrostatic stresses close to the indenter's tip were about 2.5 times lower than those for the no hardening case; however, they were 20% higher close to the residual plastic boundary. Again, this result is very relevant when crack formation is considered and will be further discussed at the end of this section. The residual compressive hydrostatic stress was 20% lower and appeared at 2.5 times deeper below the indenter's tip than for the no hardening case.

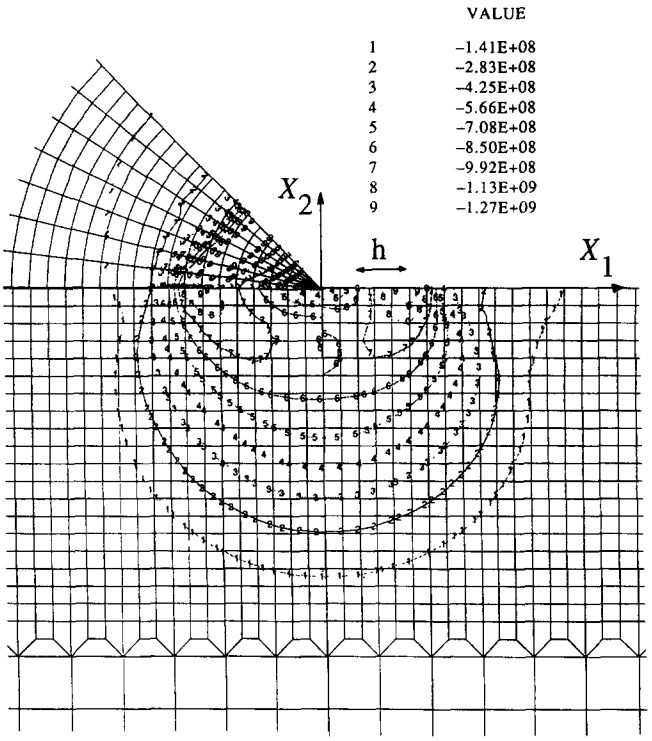

Fig. 16. Steady state hydrostatic stress (p) for aluminium 7075-T6 with plastic strain hardening $[H(\sigma_u^+) = H(\sigma_u^-)]$ at maximum load. Units are in Pa. $H/E = 0.028$, $\sigma_y/E = 0.0058$, $\sigma_y = 415.7$ MPa. The indentation depth h is also shown.

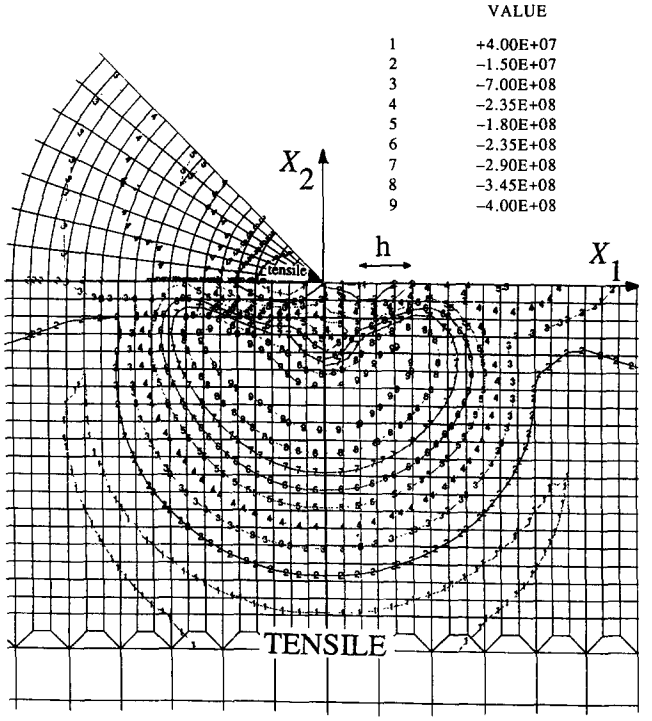

Fig. 17. Hydrostatic stress (p) for aluminium 7075-T6 with plastic strain hardening $[H(\sigma_u^+) = H(\sigma_u^-)]$ after complete unloading from steady state at maximum load. Units are in Pa. $H/E = 0.028$, $\sigma_y/E = 0.0058$, $\sigma_y = 415.7$ MPa. The indentation depth h is also shown.

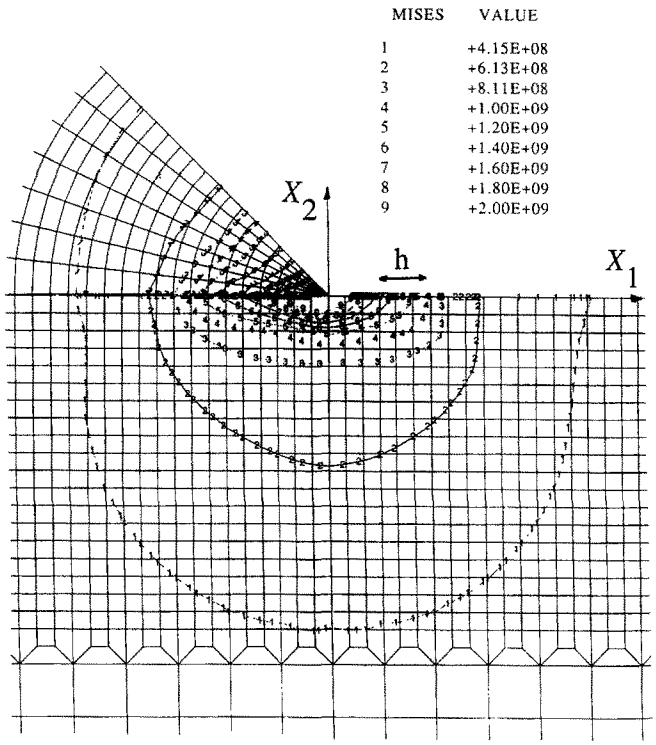

Fig. 18. Steady state Mises effective stress (σ_e) for aluminium 7075-T6 with plastic strain hardening $[H(\sigma_u^+) = H(\sigma_u^-)]$ at maximum load. Units are in Pa. $H/E = 0.028$, $\sigma_y/E = 0.0058$, $\sigma_y = 415.7$ MPa. The indentation depth h is also shown.

As regards the Mises stress (σ_e), certain similarities with the elastic solution can be seen (compare Figs 5 and 18). Compared with the no hardening case (Fig. 11), the isobars of the Mises stress at loading (Fig. 18) are different close to the indenter's tip; the maximum value appears only at the tip and the distribution follows a more regular pattern. The Mises stress isobars for 7075-T6 at unloading are shown in Fig. 19. The maximum residual Mises stress ($1.26\sigma_y$) appears at the surface, a distance of $3.5h$ away from the indenter's tip.

In summary, the results are little influenced by the Poisson's ratio, but depend on the strain hardening. For $\sigma_y/E = 0.0058$ and for the particular strain hardening $H/E = 0.028$ Figs 16–19 become universal, if the coordinates are normalized by the indentation depth h, and the stresses at loading by p_{av} (and by E for unloading). As also for the no strain hardening case, the homogeneity of the stress–infinitesimal strain relation implies a self similar solution at constant hardening.

From the present analysis it is clear that tensile stresses develop very close to the indenter's tip during loading and unloading and also along the indenter's diagonal edges. Residual tensile stresses also appear exactly below the residual plastic zone at unloading. Although the present results (using Mises plasticity) may not be relevant for glasses and ceramics, they support experimental observations [e.g. Cook and Pharr (1990)] of indentation induced macrocracks formed in such materials. Specifically, our results indicate tensile stresses that may be responsible for Palmqvist surface cracks emanating from the indentation edges and for the lateral crack which appears below the indented surface at unloading. Tensile stresses may not be the only reason for indentation induced cracking. Large inelastic shear strains were found in the present analysis which may also be responsible for indentation induced cracking. Hardening was found to lower the effective shear stresses and to increase the tensile hydrostatic stresses at the residual plastic zone. The present results confirm most of the assumptions various investigators have used to explain and to model indentation induced cracking of brittle materials, however, they do not entail rigorous proof. Brittle materials follow constitutive laws that await a more detailed indentation analysis. The results of the present analysis suggest the following fracture sequence during

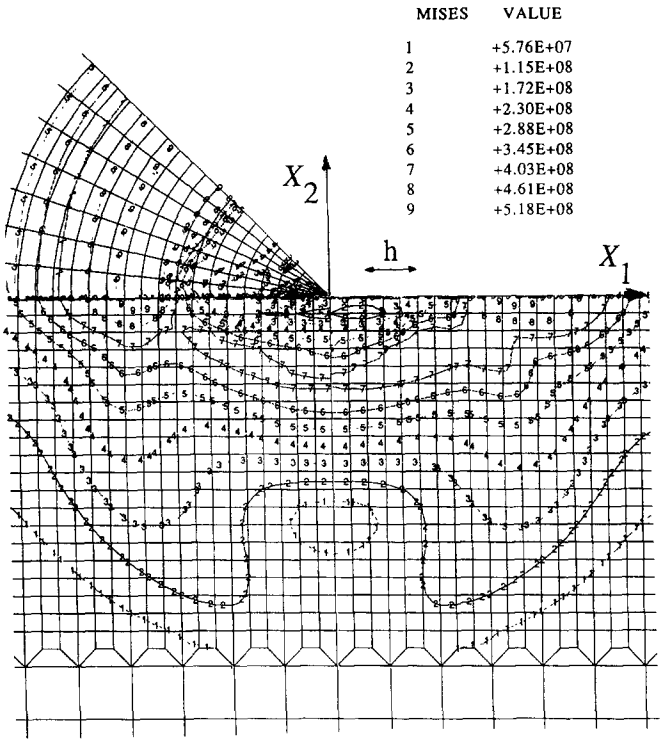

Fig. 19. Mises effective stress (σ_e) for aluminium 7075-T6 with plastic strain hardening $[H(\sigma_u^+) = H(\sigma_u^-)]$ after complete unloading from steady state at maximum load. Units are in Pa. $H/E = 0.028$, $\sigma_y/E = 0.0058$, $\sigma_y = 415.7$ MPa. The indentation depth h is also shown.

Vickers indentation: median half-penny shaped cracks are initiated at loading and continue to grow along the imprint diagonals during unloading; lateral cracks are nucleated close to the residual plastic zone boundary, beneath the indented surface, at unloading.

Finally, large strain plastic analyses of the problem were performed. For comparison, the same indentation depth was taken as for the small strain calculations. Of particular interest are the calculations done using the constitutive behaviour pertinent to aluminium 7075-T6 with small strain hardening that corresponds to constant ultimate compressive stress in the large deformation analysis and with the same elastic constants. In short, the small strain results were basically confirmed, even though for this particular case the resulting force P at a given value of indentation depth h proved to be larger, but less than 10%, compared to the small strain results. The contact area, however, did not change at all when nonlinear kinematics were considered which implies that the computed average contact pressure (hardness) is only affected by the increasing load value due to large strain analysis. The accumulated plastic strains were 11% smaller than those of the small strain formulation. The deformation mode, in this case sinking-in, at the contact contour was unaffected by the nonlinear kinematics. The Cauchy stresses were 30% larger than those computed by the small strain analysis. Near self similarity of the results was found for loads up to $0.5Eh^2$ (we did not carry out computations for higher loads). In addition to the amplitude, the fields resemble those of the small strain hardening analysis.

Evidently, both the elastic and the elastoplastic analyses show that small and large strain formulation give comparable bulk results, but are different in details regarding, for example, the magnitude of the mechanical fields involved. This finding is somewhat surprising considering the high strains involved during a Vickers indentation but is similar to results derived for the Brinell indentation. In this context, Bower *et al.* (1993) concluded by aid of FEM that a small strain analysis is sufficient for values of the ratio a/D smaller than 0.2, regardless of the strain hardening (a is the contact radius and D is the diameter of the indenting rigid sphere). Even though that analysis was performed for power-law creeping materials, a similar situation would be expected for plastic indentation. When

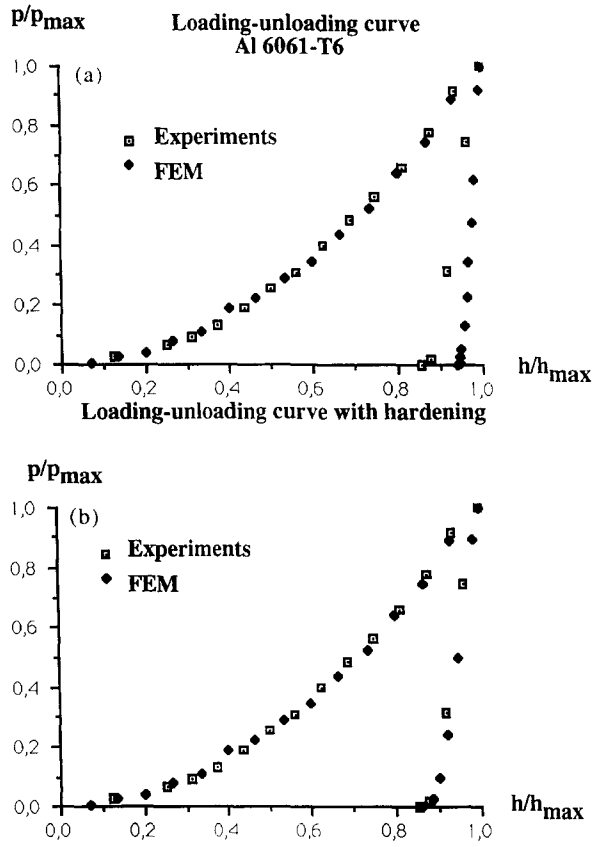

Fig. 20. Normalized load versus normalized indentation depth for Vickers test of Al 6061-T6. Experimental results by Pharr and Cook (1990). FEM results for (a) no strain hardening, (b) constant compressive strain hardening, $H(\sigma_u^+) = H(\sigma_u^-)$.

examining this result further, $a/D = 0.2$ gives a rotation at the contact contour of the spherical indenter that is 23° which in fact is a little higher than that of Vickers indentation (22°). Furthermore, the strains involved in the Brinell analysis are also very high (51%) and comparable to the Vickers indentation shown in Fig. 13 (equivalent plastic strain of 10% extends more than half the contact radius away from the contact area). Therefore, the present results, together with the results by Bower *et al.* (1993), conclude that a small strain formulation with the appropriate strain hardening provides correct basic features (e.g. force–indentation depth relation and stress and strain gradients) when analysing these standard indentation problems.

5. COMPARISON WITH EXPERIMENTS

Pharr and Cook (1990) have tested the 6061-T6 aluminium and shown the P–h relation for the Vickers indentation test (Fig. 20). The present numerical simulation provides the total load at each loading or unloading step, as the depth-sensing indentation instruments do. The applied indentation depth h, is normalized by the final maximum depth h_{max}, and the resulting force P is normalized by the maximum force P_{max} that corresponds to h_{max}. For the loading part of the curve the numerical and the experimental curves seem to be very alike, almost on top of each other. The maximum force, if computed with no strain hardening, is within 5% of the experimental maximum forces. For unloading, in particular close to full unloading, there is some discrepancy between the numerical and the experimental curves. To settle the issue, we performed uniaxial tensile tests for aluminium 6061-T6 (for 7075-T6 we used results by Hallbäck, 1993) which indicate linear strain hardening

for plastic compressive strains in the range of 0.3. Further analysis showed that the discrepancy in the unloading part of the P–h curve can be completely eliminated [Fig. 20(b)], if the numerical curve is computed by taking a constant hardening tangent to the σ–ε compression curve at σ_u [Fig. 8(c)]. It may be concluded that the unloading branch of the load–depth curve can be simulated well, only if the correct compressive strain hardening is taken into account. The net area enclosed by the P–h curve is a measure of the plastic dissipation of the material [e.g. by integrating eqn (29)]. Similar to Pharr and Cook (1990) experimental results were observed by us (Larsson *et al.*, 1994), for aluminium 7075-T6, 6061-T6, tungsten and tantalum. Low strain hardening results in bringing the final part of the unloading branch of the P–h curve closer to the loading branch, as the experiments also indicate.

As regards comparison of hardness values, the experimental Vickers hardness reported by Pharr and Cook (1990) for aluminium 6061-T6 was 1.1 GPa. The computed hardness for aluminium 6061-T6 assuming zero strain hardening was found to be 0.7 GPa. However, when a constant hardening tangent was considered, the computed hardness [eqn (28)] was 1.04 GPa which is in good agreement with the experimental hardness given above. This is further underlined by the fact that this result is calculated using a small strain formulation and, as discussed in Section 4.2, the large strain formulation gives a somewhat higher value for the computed hardness, almost identical to the experimental one. Therefore, eqn (28) and the accompanying discussions may serve as a good estimate of hardness when the relative material properties are known. On the other hand, if hardness, degree of pile-up and P–h output are known from a Vickers test, material properties can be inferred by using the results of the present investigation.

In the absence of hardening, the maximum principal stress at loading is found to be tensile close to the indenter's tip (about $h/2$ away from the tip), further away it becomes compressive. Therefore, "cup" type of cracking damage may be expected in the area close to the indenter's tip and edges. Such highly localized damage at loading has been experimentally observed in the Vickers indentation of polycrystalline alumina (Al_2O_3) material (Zeng and Rowcliffe, 1994a; Zeng *et al.*, 1993). At unloading (with and without strain hardening), tensile stresses at the boundary of the residual plastic volume, beneath the contact area (Figs 15 and 17) could partially explain the lateral cracks observed by Cook and Pharr (1990).

Further comparison of our numerical results was done with the work by Zielinski *et al.* (1993) who observed (with transmission electron microscopy) the dislocation evolution in a Vickers test of a Fe-3 wt% Si composite and thus measured the plastic boundary c. Their values are in good agreement with the present analysis [eqn (31)].

Indentation experiments of Söderlund to tungsten, alumina and glass indicate two regions that can be clearly distinguished from a log (P)–log (h) plot at low indentation loads: an elastic contact response due to the initial small roundness of the indenter (Söderlund and Macmillan, 1991), and an elastoplastic response due to sharp indentation which is in accordance with the present analysis. We analysed the experimental results of Söderlund (1993) and did not find any elastic response according to eqns (13) and (14). We therefore conclude that the pure elastic results are of little use in the analysis of most sharp indentation experiments on metals and ceramics. However, the experimental results give confidence that the present analysis [eqns (29) and (30)] can be very useful in order to derive both elastic and plastic constitutive parameters using both the loading and unloading path of an indentation experiment. Equation (30) is found to be a somewhat cruder approximation than eqn (29) when compared with experiments, unless unloading is done with extremely small decrements of the indentation depth at maximum indentation. For the time being, the initial unloading part of the indentation P–h relation seems to be the best way to evaluate the elastic properties of indented materials.

Zeng and Rowcliffe (1994b) have recently developed an indentation technique to measure the residual fields around Vickers indentation in glasses and ceramics. By using smaller indentations as microprobes, the surface residual stress field created by the large indentation can be tracked, based on the observation that the crack lengths of the small indentation change with the magnitude of the residual stresses. These experimental results

indicate that the indentation residual stresses scale directly with the load. The surface residual stresses were found to form a biaxial field with tensile tangential and compressive radial stress, in accordance with our numerical analysis.

6. CONCLUSIONS

Although there is a growing consciousness in the mechanics and materials community of the fundamental importance of the sharp indentation testing, there is little mechanical analysis done so far in this area. Therefore, the scope of this paper was to contribute to the analytic background on the use of sharp indenters for mechanical characterization of materials. Regarding the material response, the undertaken mechanical analysis was phenomenological; heat generation, dislocation activity in slip bands at individual grains, atomic reactions due to the sharpness of the indenter and its associate compressive stress singularity, as well as other physical responses were not accounted for. In order for the present analysis to be realistic, the indentation depth has to be much larger than any characteristic microstructural dimension of the material or the indenter (e.g. grain size and tip roundness).

In the present paper, the theoretical foundation for the Vickers hardness testing was numerically explored. The theoretical predictions concern materials that fall in the category of isotropically hardening, rate independent, isothermal, elastoplastic constitutive behavior. The influence of the material strain hardening and of the yielding stress were examined. Formulae for steady state hardness, that is hardness independent of the load, were derived. The results were compared to available experiments and proved to be in very good agreement. The elastic unloading effect on the indentation depth and shape was also examined and indicated possible crack formation in brittle materials. By studying the depth of the indentation as a function of the force on the indenter, the material hardness and stiffness can be determined. The details of the corresponding deformation and stress fields are presented for the first time. Macroscopic parameters such as load and indentation depth were found to relate with material properties such as Young's modulus, yield stress and strain hardening. Strain hardening was associated with material sinking-in. The small strain analysis was found to give the right trend for the overall load–depth behavior and the stress and strain fields as computed with large strain analysis, if the appropriate strain hardening was taken into consideration. However, the amplitudes of the fields as computed by small and large strain analysis are different.

Below, we present a synopsis of our basic results:

(1) Elastic and elastoplastic FEM analysis of the Vickers test (Fig. 1) were undertaken. Small strain and hypoelastic formulation were used, giving comparable results. Hooke's law was used for the elastic response and Prandtl–Reuss equations for elastoplasticity with and without compressive strain hardening. Certain limitations on the validity of the analysis were pointed out. Comparison with the conical punch analysis was made, revealing many similarities but also some differences with the present results.

(2) Universal steady state relations between indentation load P and indentation depth h were found for elastic [eqn (13)], and elastoplastic [eqn (29)] response for loading, the latter being more useful for experimental analysis. The average contact pressure for loading p_{av} was found for elastic [eqn (14)], and elastoplastic [eqn (28)] response, and was nearly load independent. The projected contact area was almost square for the elastoplastic behavior [Fig. 10(a)], but deviated from a square for the elastic behavior (Fig. 4). The residual imprint projection captured well the projected contact area at loading, thus, eqn (28) can be used to estimate the Vickers hardness. With the new, advanced hardness testing instruments, the P–h relation can be recorded and used for the assessment of material properties. The elastic material properties were related to the initial unloading part of the P–h curve through eqn (30). Other material properties can be inferred from a Vickers test, if the hardness, the P–h relation (at loading and unloading) and the degree of pile-up are known.

(3) The elastoplastic boundary was estimated by eqn (32). Such results may be used for further examination of the inelastic deformation mechanisms (dislocations in this case) using, for instance, transmission electron microscopy to observe cross sections of the indented specimens.

(4) At loading, a characteristic plastic strain of 0.3 was found to control the strain hardening cases, in line with what is found for the Brinell indentation. The Brinell and the Vickers tests seems to be related, as is empirically well known from experiments.

(5) The steady state mechanical stresses and deformation fields were computed for the elastic case (Figs 4–7), the elastoplastic case with no strain hardening (Figs 10–15), and with low strain hardening (Figs 16–19). The solutions appear self similar and become universal, if normalized accordingly (see Sections 3 and 4 for details). Strain hardening was found to suppress material pile-up at the contact boundary. The peak of pile-up corresponded to the edge of the contact area in the case of no strain hardening. Experimentally, pile-up is very useful in evaluating material hardness, whereas sinking-in may complicate the estimation of the contact area, henceforth, the hardness.

(6) Possible cracking locations at loading but mostly at unloading (Figs 15 and 17) were identified, in accordance with experimental observations of Vickers indentations of brittle materials. Residual tensile stresses are higher for the strain hardening case. Large inelastic shear strains could be also a reason for indentation induced cracking. Compressive strain hardening increases the residual tensile stresses. However, the present analysis is strictly valid only for metal plasticity.

(7) Some indentation size effect, that is higher average contact pressure than the steady state prediction [eqn (28)], was found at low loads. The results, although tentative to experimental hardness values at very low loads, were inconclusive about this issue. More details in the modeling (e.g. friction at the interface) are probably needed to capture this important feature of the indentation analysis. All present results appeal to steady state conditions of a Vickers test.

(8) Comparisons with available experiments of our own and of others showed very good agreement with the present analysis. Full agreement was achieved only when large strains and the correct hardening were taken into account.

General results such as the ones derived in this work can serve many purposes. Corrections of existing empirical hardness formulae may be attempted in order to retain the wealth of existing experimental information on many structural materials already developed and used. Assessment of microdeformation mechanisms will further explain different failure modes induced by Vickers (or other sharp indentation) like, for example, compaction and phase transformation (pressure sensitivity), cracking (maximum tensile stress), and plasticity due to dislocation activity (maximum effective shear stress). Finally, the possibility of optimization of the indenter's shape in order to minimize (or maximize) the damage induced or to accelerate the steady state hardness will be investigated for future suggestions on indentation tests.

Acknowledgements—The authors would like to thank Prof. B. Häggblad, Miss E. Söderlund, Dr K. Zeng, Prof. D. Rowcliffe and Mr S. Biwa for most helpful discussions. We would like to thank Mr H. Öberg for very able experimental assistance. The use of CRAY X-MP/416 supercomputer at the Linköping University was made possible by the National Supercomputer Centre of Sweden.

REFERENCES

ABAQUS (1989). Users' Manual, Version 4.8. Hibbitt, Karlsson & Sorensen.

Anstis, G. R., Chantikul, P., Lawn, B. R. and Marshall, D. B. (1981). A critical evaluation of indentation techniques for measuring fracture toughness: I. Direct crack measurement. *J. Am. Ceram. Soc.* **64**(9), 533–538.

Bhattacharya, A. K. and Nix, W. D. (1988a). Finite element simulation of indentation experiments. *Int. J. Solids Structures* **24**, 881–891.

Bhattacharya, A. K. and Nix, W. D. (1988b). Analysis of elastic and plastic deformation associated with indentation testing of thin films on materials. *Int. J. Solids Structures* **24**, 1287–1298.

Bilodeau, G. G. (1992). Regular pyramid punch problem. *J. Appl. Mech.* **59**, 519–523.

Bower, A. F., Fleck, N. A., Needleman, A. and Ogbonna, N. (1993). Indentation of a power law creeping solid. *Proc. R. Soc. Lond.* **A441**, 97–124.

Cook, R. F. and Pharr, G. M. (1990). Direct observation and analysis of indentation cracking in glasses and ceramics. *J. Am. Ceram. Soc.* **73**(4), 787–817.

Evans, A. G. and Charles, E. A. (1976). Fracture toughness determination by indentation. *J. Am. Ceram. Soc.* **59**(7–8), 371–372.

Hallbäck, N. (1993). Licenciate Thesis, Royal Inst. Tech., Stockholm, Sweden.

Hill, R., Storåkers, B. and Zdunek, A. B. (1989). A theoretical study of the Brinell hardness test. *Proc. R. Soc. Lond.* **A423,** 301–330.

Johnson, K. L. (1970). The correlation of indentation experiments. *J. Mech. Phys. Solids* **18,** 115–126.

Johnson, K. L. (1985). *Contact Mechanics.* Cambridge University Press, Cambridge.

Kikuchi, N. and Oden J. T. (1988). *Contact Problems in Elasticity: A Study of Variational Inequalities and Finite Element Methods.* SIAM, Philadelphia.

King, R. B. (1987). Elastic analysis of some punch problems for a layered medium. *Int. J. Solids Structures* **23**(12), 1657–1664.

Larsson, P.-L., Söderlund, E., Giannakopoulos, A. E., Rowcliffe, D. J. and Vestergaard, R. (1994). Analysis of Berkovich indentation, in preparation.

Laursen, T. A. and Simo, J. C. (1992). A study of microindentation using finite elements. *J. Mater. Res.* **7,** 618–626.

Lawn, B. R., Evans, A. C. and Marshall, D. B. (1980). Elastic/plastic indentation damage in ceramics: the median/radial crack system. *J. Am. Ceram. Soc.* **63**(9–10), 574–581.

Lesko, J. J., Garman, G. P., Dillard, D. A., Reifsnider, K. L. and Stinchcomb, W. W. (1991). Indentation testing of composite materials: a novel approach to measuring interfacial characteristics and engineering properties. CCMS-91-12. Rep. of Engng Science and Mech., Virginia Polytech. Inst. and State Univ.

Li, H., Ghosh, A., Hom, Y. H. and Brandt, R. C. (1993). The frictional component of the indentation size effect in low load microhardness testing. *J. Mater. Res.* **8**(5), 1028–1032.

Maiden, C. J. and Green, S. J. (1966). Compressive strain-rate tests on six selected materials at strain rates from 10^{-3} to 10^{4} in/in/sec. *J. Appl. Mech.* **88,** 496–504.

Mott, B. W. (1956). *Micro-Indentation Hardness Testing.* Butterworths, London.

Nagtegaal, J. C. and de Jong, J. E. (1982). Some aspects of nonisotropic work hardening in finite plasticity. *Proc. Workshop on Plasticity of Metals at Finite Strain,* pp. 66–106. Div. Appl. Mech., Stanford University.

Needleman, A. (1972). A numerical study of necking in circular cylindrical bars. *J. Mech. Phys. Solids* **20,** 111–127.

Olaf, J. M. (1993). Finite element analysis of indentation experiments. *Proc. 1st Int. Conf. Contact Mech.,* pp. 69–76.

Pethica, J. B., Hutchings, R. and Oliver, W. C. (1983). Hardness measurements at penetration depths as small as 20 nm. *Philos. Mag.* **A48,** 593–606.

Pharr, G. M. and Cook, R. F. (1990). Instrumentation of a conventional hardness tester. *J. Mater. Res.* **15**(4), 847–851.

Sneddon, I. N. (1945). Boussinesq's problem for a flat-ended cylinder. *Proc. Cambridge Philosophical Soc.* **42,** 29–39.

Sneddon, I. N. (1965). The relation between load and penetration in the axisymmetric Boussinesq problem for a punch of arbitrary profile. *Int. J. Engng Sci.* **3,** 47–57.

Söderlund, E. (1993). Unpublished results.

Söderlund, E. and Macmillan, N. H. (1991). Analysis of the differential (alternative current) technique for measuring Young's modulus during ultra-low load indentation. *J. Mater. Sci. Letters* **10,** 720–722.

Storåkers, B. and Larsson, P.-L. (1993). On Brinell and Boussinesq indentation of creeping solids. *J. Mech. Phys. Solids* **42,** 307–332.

Tabor, D. (1951). *Hardness of Metals.* Clarendon Press, Oxford.

Wang, H. and Bangert, H. (1993). Three-dimensional finite element simulation of Vickers indentation on coated systems. *Mater. Sci. Engng* **A163,** 43–50.

Williams, M. L. (1952). Stress singularities resulting from various boundary conditions in angular corners of plates in extension. *J. Appl. Mech.* **74,** 526–528.

Zeng, K. and Rowcliffe, D. (1994a). Identification of fracture sequences during sharp indentation of polycrystalline alumina. *J. Mater. Res.,* in press.

Zeng, K. and Rowcliffe, D. (1994b). Experimental measurement of residual stress field around a sharp indentation in glass. *J. Am. Ceram. Soc.* **77,** 524–530.

Zeng, K., Breder, K. and Rowcliffe, D. (1993). Comparison of slow crack growth in alumina and SiC-whisker-reinforced alumina. *J. Am. Ceram. Soc.* **76**(7), 1673–1680.

Zielinski, W., Huang, H. and Gerberich, W. W. (1993). Microscopy and microindentation mechanics of single crystal Fe-3 wt% Si: Part II. TEM of the indentation plastic zone. *J. Mater. Res.* **8**(6), 1300–1310.